Moist Baroclinic Instability along the Subtropical Mei-Yu Front

GUANG YANG[a] AND TIM LI[a,b]

[a] *Department of Atmospheric Sciences, School of Ocean and Earth Science and Technology, University of Hawai'i at Mānoa, Honolulu, Hawaii*

[b] *Key Laboratory of Meteorological Disaster, Ministry of Education, Joint International Research Laboratory of Climate and Environmental Change, Collaborative Innovation Center on Forecast and Evaluation of Meteorological Disasters, Nanjing University of Information Science and Technology, Nanjing, China*

(Manuscript received 7 March 2022, in final form 27 September 2022)

ABSTRACT: Differing from classic midlatitude dry baroclinic instability theory, atmospheric motions over the subtropical mei-yu front in boreal summer are dominated by synoptic-scale disturbances coupled with precipitation and moisture under a weaker background vertical shear. This moisture–precipitation–circulation interactive feature, along with a preferred zonal wavelength of about 3400 km and eastward phase propagation, is explained by a moist baroclinic instability theoretical framework. The new framework is an extension of a traditional two-level baroclinic model by considering a prognostic moisture equation, the moisture–precipitation–circulation feedback, and an interactive planetary boundary layer. An eigenvalue analysis of the model shows that the most unstable mode has a preferred zonal wavelength of 3400 km, a westward-tilted vertical structure, and a phase leading of maximum moisture and precipitation anomalies relative to a lower-tropospheric trough, all of which are in good agreement with observations. Both anomalous horizontal and vertical advection processes contribute to the moisture increase. Further sensitivity tests show that the instability and the zonal-scale selection primarily arise from the moisture–convection–circulation feedback, while the vertical shear provides an additional energy source for the perturbation growth. This moist baroclinic instability theory explains well the observed characteristics of the development of synoptic-scale disturbances along the mei-yu front.

KEYWORDS: Instability; Mei-yu fronts; Baroclinic models

1. Introduction

Dominant perturbations in midlatitudes during boreal winter are baroclinic synoptic-scale waves along 40°–50°N with a westward-tilted vertical structure and a typical zonal wavelength of 4000–6000 km (Holton 2004). Due to an extremely strong westerly jet associated with a large meridional temperature gradient in boreal winter, the synoptic-scale perturbations directly gain energy from the mean kinetic and potential energy without the involvement of diabatic heating (Pedlosky 1964; Smagorinsky et al. 1965; Fowlis and Hide 1965). The observed synoptic-scale motions are well explained by the classic baroclinic instability theory. The original baroclinic instability models such as Charney (1947) and Eady (1949) used a vertically continuous model with an idealized density vertical profile. Phillips (1954) developed a two-level model to describe midlatitude baroclinic waves. While this model only resolves the lowest vertical mode, it provides more clear physical pictures for the preferred scale selection, vertical structure, the role of the secondary circulation in regulating the hydrostatic approximation and the geostrophic balance, and energetics for the growth of synoptic-scale disturbances.

The original baroclinic instability theory did not incorporate diabatic heating. It was extended later with condensational heating, which was parameterized in terms of an integral relationship between the baroclinically induced vertical velocity at a low level and the vorticity field (Mak 1982). The Charney model was extended to study the dynamics of transient planetary waves by including Newtonian cooling, Ekman dissipation, and a linear vertical variation of the stratification parameter (Wang et al. 1985). A general dispersion relation and eigenfunction were derived analytically for a midlatitude zonal flow with a conditionally unstable layer in the presence of the Ekman layer (Wang and Barcilon 1986). A two-level model with the semigeostrophic approximation was developed for slantwise moist convection-induced baroclinic instability in a weak hydrostatic stability environment (Emanuel et al. 1987). A two-dimensional numerical model was used to study moist baroclinic instability based on the constraints of slantwise convectively neutral basic state and uniform shear (Fantini 1993). Whether moist baroclinic instability is responsible for the growth of monsoon depressions was examined with a conceptual model that specified a moist, baroclinic basic state (Cohen and Boos 2016).

In contrast to the wintertime synoptic-scale disturbances induced by dry baroclinic instability, dominant midlatitude perturbations, coupled with large moisture content and strong precipitation, are eastward-propagating synoptic-scale waves along the subtropical front (around 30°N) in boreal summer. The subtropical front is extremely strong over East Asia during summer and is often termed as the mei-yu in China, baiu in Japan, and changma in the Korean Peninsula (Chen and Chang 1980; Wang et al. 2003; Choi et al. 2020). Climatologically, the monsoon rain belt moves slowly northward as the season progresses. The mei-yu rain belt typically occurs along the Yangtze River in central China from early June to early July, and it stretches farther eastward to southern Japan and

Corresponding author: Tim Li, timli@hawaii.edu

DOI: 10.1175/JCLI-D-22-0140.1

the western North Pacific along the northwestern rim of the North Pacific subtropical high (NPSH; Ding 1992; Wang and Lin 2002; Ding 2007; Day et al. 2018). Synoptic-scale disturbances, which originate from "southwest vortices" over the eastern flank of the Tibetan Plateau, develop rapidly along the mei-yu front and may cause devastating floods in the region as they propagate eastward (Gao et al. 2002; Yue et al. 2003; Liu et al. 2003).

So far there have been no appropriate theories explaining the moist baroclinic instability along the mei-yu front. The development of synoptic-scale perturbations along the mei-yu front in boreal summer is significantly different from those grown as a result of dry baroclinic instability. First, the vertical shear and meridional temperature gradient in summer are not as strong as in winter. Therefore, the baroclinic instability associated with the summer westerly jet is weaker. Second, due to the great moisture amount and strong precipitation along the subtropical mei-yu front, the moistening process in connection with condensational heating cannot be ignored.

The objective of this study is to provide a theoretical framework of moist baroclinic instability applicable to the synoptic-scale disturbances along the summer subtropical front. A key feature of this theoretical framework is the consideration of a moisture–precipitation–circulation feedback under a proper vertical shear environment. Thus, this theoretical framework concerns moist baroclinic dynamics of synoptic-scale disturbances with a combined tropical and midlatitude feature. It is anticipated that under this new dynamical regime, the most unstable perturbations would gain energy from both the baroclinicity of atmosphere and the moisture related to condensational heating.

The remaining part of this paper is organized as follows: a brief description of the data and the model is given in section 2. Section 3 describes the observed structure and evolution of synoptic-scale disturbances along the mei-yu front. A theoretical moist baroclinic model based on the quasigeostrophic framework and a prognostic moisture equation is developed in section 4, and the eigensolutions of the moist baroclinic model are presented in section 5. The sensitivity of the model solution to key parameters such as background vertical shear and the diabatic heating coefficient is further discussed in section 6. Finally, a summary and discussion are presented in the last section.

2. Data and methods

Daily precipitation data from the Global Precipitation Climatology Project (GPCP; Huffman et al. 2001) dataset were employed in this study. The period of the daily precipitation dataset is from 1997 to 2020 at a spatial resolution of $1° \times 1°$. In addition, we used the fifth major global reanalysis produced by the European Centre for Medium-Range Weather Forecasts (ECMWF) (ERA5; Hersbach et al. 2019) with a horizontal resolution of $0.25° \times 0.25°$. This dataset includes hourly precipitation, specific humidity, geopotential height, divergence, vertical velocity, and wind fields from 1979 to 2020.

As we focus on the synoptic-scale perturbations during the mei-yu season, the data in June and July were particularly selected. The synoptic-scale disturbances were derived by applying a 2–10-day bandpass filter to the original datasets. For comparison, we also analyzed the intraseasonal component, which was defined as a signal with a period of 10–90 days. The climatological annual cycle was removed first from the original data before the temporal decomposition was applied.

A theoretical model was constructed to understand the moist baroclinic instability along the mei-yu front. The model was based on the conventional two-level model for the midlatitude baroclinic instability problem (Holton 2004) and was extended by including a lower-tropospheric moisture tendency equation and a planetary boundary layer (PBL) in which the pressure gradient force is balanced by the Coriolis force and frictional force (e.g., Wang and Li 1993). In the theoretical model, an idealized background mean state is specified, and a total variable is decomposed into two parts: a basic state component and a perturbation component.

A modified Betts–Miller (Betts 1986; Betts and Miller 1986) convective parameterization scheme was employed, following Wang and Chen (2017). Although simple, this theoretical model allows the moisture–convection–circulation feedback and PBL-free atmospheric circulation interaction.

3. Observed characteristics of synoptic-scale disturbances along the mei-yu front

Before constructing a theoretical model, we first illustrate the observed characteristics of synoptic-scale disturbances along the mei-yu front in June and July. The top panels of Fig. 1 show the standard deviation maps of daily precipitation anomalies from the GPCP and ERA5 datasets. The main activity center of the daily precipitation variability is located south of 35°N in East Asia, extending over a wide area from the southeast coast to the North China Plain (Figs. 1a,d). The maximum standard deviation is about 20 mm day^{-1}, which is close to the climatological-mean value along the mei-yu front (around 30°N). This indicates that the rainfall variability over the subtropical front is very strong.

To illustrate the relative contribution of synoptic-scale and intraseasonal components to the total rainfall variability, we show the standard deviation maps of synoptic-scale and intraseasonal precipitation anomalies in the lower panels of Fig. 1. It is clear that the largest contribution of the regional rainfall variability arises from the synoptic-scale component. On the synoptic time scale, the variation of precipitation is most pronounced near 30°N in eastern China. The major activity center of synoptic-scale component of precipitation anomalies is confined in the middle and lower reaches of the Yangtze River, with maximum variability of the synoptic-scale component of precipitation anomalies located near 30°N, 117°E for both GPCP dataset and ERA5 reanalysis (Figs. 1b,e).

The intraseasonal components of precipitation are weaker along the subtropical mei-yu front, and its major activity center appears south of 33°N over southeast China (Figs. 1c,f). The amplitude and relative strength of precipitation standard deviation fields shown in Figs. 1a–c in general resemble those

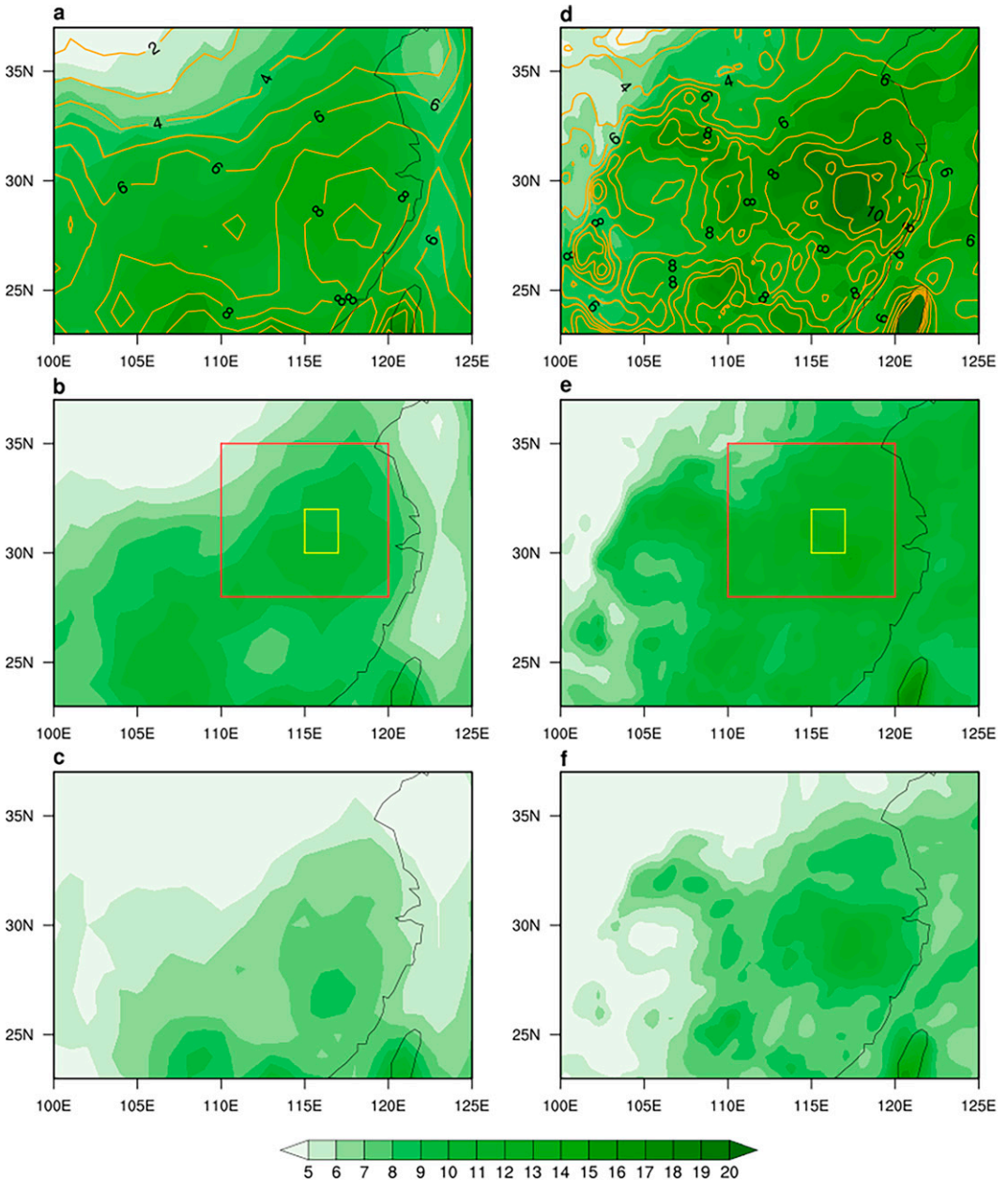

FIG. 1. (a),(d) The climatological-mean precipitation field (contour; mm day^{-1}) and the standard deviation of daily precipitation anomalies (shading; mm day^{-1}) from the (left) GPCP dataset and the (right) ERA5 reanalysis. (b),(c),(e),(f) The standard deviation of corresponding synoptic-scale and intraseasonal components of the precipitation anomalies. The red and yellow boxes denote the regions with maximum synoptic-scale variability along the mei-yu front.

shown in Figs. 1d–f, suggesting that the variability of precipitation from the GPCP dataset is consistent with that from the ERA5 reanalysis. This indicates that the intraseasonal variability is comparatively unimportant over the mei-yu front region. As a result, the synoptic-scale component of precipitation dominates the variability of mei-yu precipitation.

To quantitatively measure the relative contribution of the synoptic-scale and intraseasonal components, we used two boxes to represent the maximum rainfall variability region along the mei-yu front: a red box indicates region 1 (110°–120°E, 28°–35°N), and a yellow box indicates region 2 (115°–117°E, 30°–32°N). Table 1 shows the percentage of the box-averaged synoptic-scale and intraseasonal precipitation standard deviations to the total standard deviation. In both the red and yellow boxes, the synoptic-scale component is about 70% of the total precipitation variability, while the intraseasonal component is relatively

TABLE 1. Percentage of contributions by the synoptic-scale P_1 and intraseasonal P_2 components to the total precipitation variability averaged over the red and yellow boxes shown in Fig. 1b. The results are from the GPCP and ERA5 reanalysis datasets.

		P_1	P_2
Region 1	GPCP	71%	50%
	ERA5	70%	51%
Region 2	GPCP	71%	49%
	ERA5	70%	51%

weak (50%). The percentage of the relative contributions in region 1 is approximately equal to that in region 2, and the result is consistent for the GPCP and ERA5 datasets. This again suggests that the synoptic-scale disturbances are the dominant weather system along the subtropical mei-yu front.

Next, the structure and evolution of the synoptic-scale disturbances along the mei-yu front were examined. Figure 2 shows the temporally evolving patterns of synoptic-scale precipitation, 850-hPa wind, specific humidity, and 200-hPa wind fields regressed onto the synoptic-scale precipitation time series at a reference point (30°N, 117°E). A clear eastward-propagating feature is manifested from day −2 to day +1. As the synoptic-scale disturbances move eastward, they are enhanced from day −2 to day 0 and then decay gradually from day 0 to day +1.

On day −2, a weak positive precipitation center is located at 105°E, while a negative center appears over the reference point, accompanied by lower-level anticyclonic circulation. The specific humidity field in general resembles the precipitation pattern, with a weak positive value to the west and a negative center to the east (Figs. 2a,e). On day −1, the positive precipitation perturbations strengthen markedly with a strong activity center at 30°N, just to the east of 110°E, whereas the negative precipitation perturbations decrease in strength. A cyclonic vortex at the lower level develops over the region of positive precipitation (Figs. 2b,f).

On day 0, the positive precipitation and specific humidity perturbations peak at the reference point. The northeast–southwest-tilted precipitation field is accompanied by the large-scale low-level cyclonic circulation. The southwesterly flow to the south of the cyclone advects high-mean moisture northward, strengthening the precipitation anomalies. Due to horizontal and vertical moisture advection, the maximum specific humidity field is approximately in phase with the precipitation field, also showing a northeast–southwest-tilted pattern. An anomalous anticyclonic circulation appears in the upper troposphere, clearly indicating a baroclinic structure. The zonal extent of the maximum precipitation center on day 0 extends from southwest China all the way to the East China Sea (Figs. 2c,g).

On day +1, the positive precipitation and specific humidity centers continue moving eastward into the western Pacific, and the anomalous lower-level and upper-level circulation shift similarly. The synoptic-scale disturbances weaken as they move farther eastward (Figs. 2d,h).

The tight coupling among synoptic-scale low-level cyclonic circulation, moisture, and precipitation fields is clearly demonstrated from the evolution patterns shown in Fig. 2. To illustrate the vertical structure of the observed synoptic-scale disturbances along the mei-yu front, we plotted the zonal–vertical cross sections of synoptic-scale vertical velocity, divergence, specific humidity, and geopotential height fields along 32°N from day −2 to day +1 (Fig. 3). The most striking feature is the first baroclinic mode in the divergence field, that is, a lower-level convergence and an upper-level divergence, is in phase with the midtropospheric ascending motion (Figs. 3a–d). The geopotential height field exhibits a clear vertically tilting structure toward the west with height (Figs. 3e–h). The maximum anomalous specific humidity center is located in the lower troposphere around 700 hPa. It shifts slightly to the east of the low-level trough, implying the critical roles of anomalous meridional and vertical moisture advection associated with Ekman pumping-induced ascending motion at the top of PBL in the change of specific humidity.

The zonal wavelength of the observed synoptic-scale disturbances along the mei-yu front may be estimated from the zonal–vertical profiles of the geopotential height on day 0 (Fig. 3g), when the intensity of the synoptic-scale motions reaches a maximum. It is about 35° in longitude from one ridge to another, which is about 3400 km. The zonal phase speed of the synoptic-scale perturbations may be estimated based on the maximum specific humidity centers from day −1 to day +1. It is about 18° in longitude between day −1 and day +1, which corresponds to a zonal phase speed of 10 m s^{-1}.

4. Construction of a moist baroclinic model

Given the unique feature of synoptic-scale disturbances along the subtropical mei-yu front, we intend to construct a theoretical model that involves both the midlatitude quasigeostrophic dynamics and extratropical moistening processes. Consider a 2.5-layer model with conventional two-level model in the free atmosphere and a well-mixed PBL. The geostrophic wind can be expressed as

$$V_\psi = \mathbf{k} \times \nabla\psi,$$

where $\mathbf{k}$ designates a vertical unit vector, and ψ is the geostrophic streamfunction.

The vorticity and thermodynamic equations in the free atmosphere may be written as

$$\frac{\partial}{\partial t}\nabla^2\psi + V_\psi \cdot \nabla(\nabla^2\psi) + \beta\frac{\partial\psi}{\partial x} = f_0\frac{\partial\omega}{\partial p}, \tag{1}$$

$$\frac{\partial}{\partial t}\left(\frac{\partial\psi}{\partial p}\right) = -V_\psi \cdot \nabla\left(\frac{\partial\psi}{\partial p}\right) - \frac{\sigma}{f_0}\omega - \frac{\kappa\dot{Q}}{f_0 p}, \tag{2}$$

where ω represents the vertical velocity, Q denotes the diabatic heating rate per unit mass, κ is the ratio of gas constant to specific heat at constant pressure, and f_0 is the Coriolis parameter.

Following Holton (2004), we use the conventional notion that levels 0, 1, 2, 3, and 4 denote the top of the atmosphere, upper troposphere, midtroposphere, lower troposphere, and top of PBL, respectively. Assume that the vertical velocity at

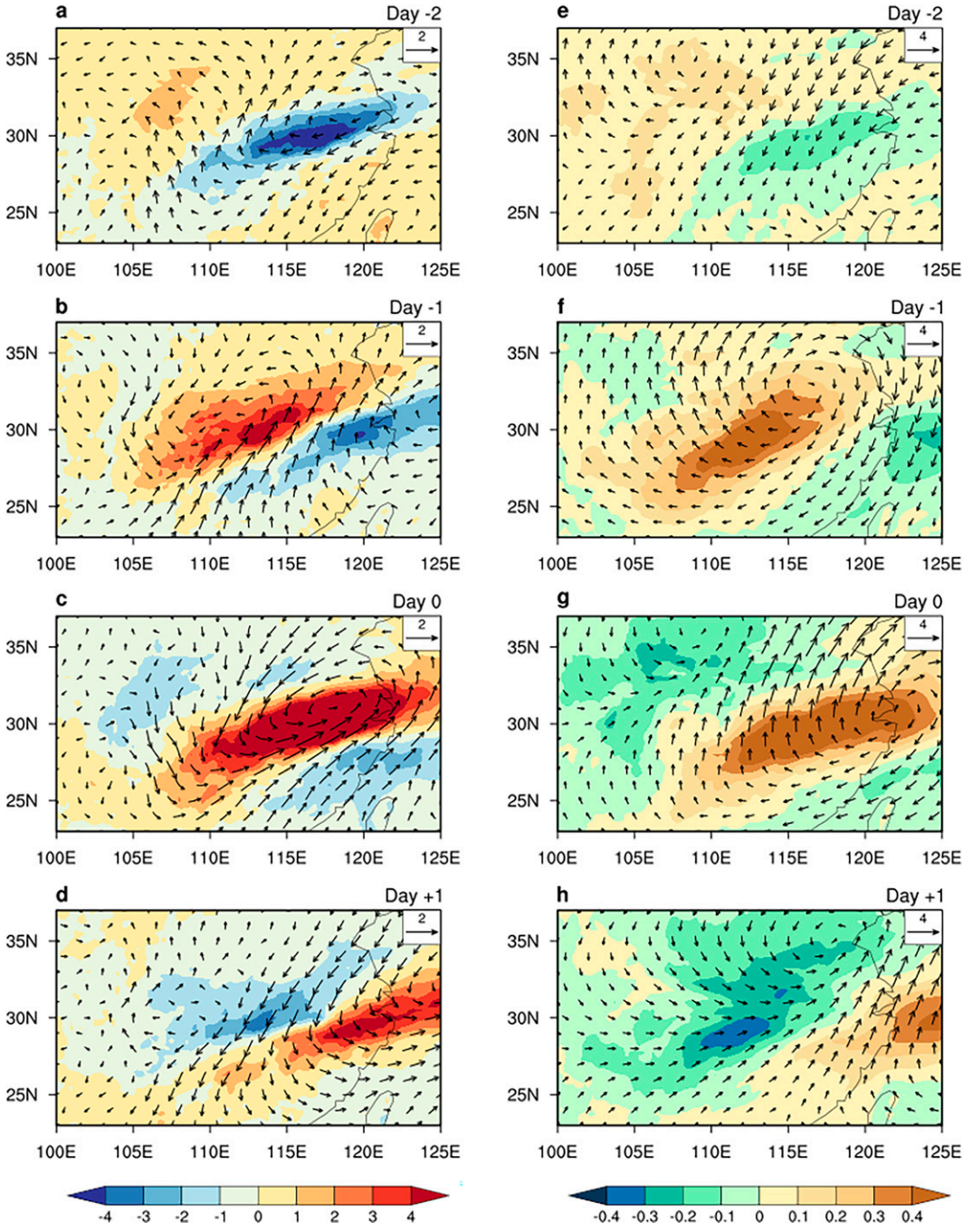

FIG. 2. (a)–(d) Horizontal patterns of regressed synoptic-scale precipitation (shading; mm day^{-1}) and 850-hPa wind (vector; m s^{-1}) fields from day −2 to day +1 for the ERA5 reanalysis. (e)–(h) As in (a)–(d), but for synoptic-scale specific humidity (shading; g kg^{-1}) and 200-hPa wind (vector; m s^{-1}).

the top of the free atmosphere vanishes ($\omega_0 = 0$). At the top of the PBL, the Ekman pumping-induced vertical velocity is determined by the relative vorticity the same level, and it can be expressed as

$$\omega_4 = -\alpha\nabla^2\psi, \tag{3}$$

where α represents the Ekman pumping coefficient.

One may write the vorticity equation at levels 1 and 3 and the thermodynamic equation at level 2. The vertical gradient of vertical velocity at levels 1 and 3 can be estimated using a finite difference method as following:

$$\left(\frac{\partial\omega}{\partial p}\right)_1 \approx \frac{\omega_2 - \omega_0}{\delta p},$$

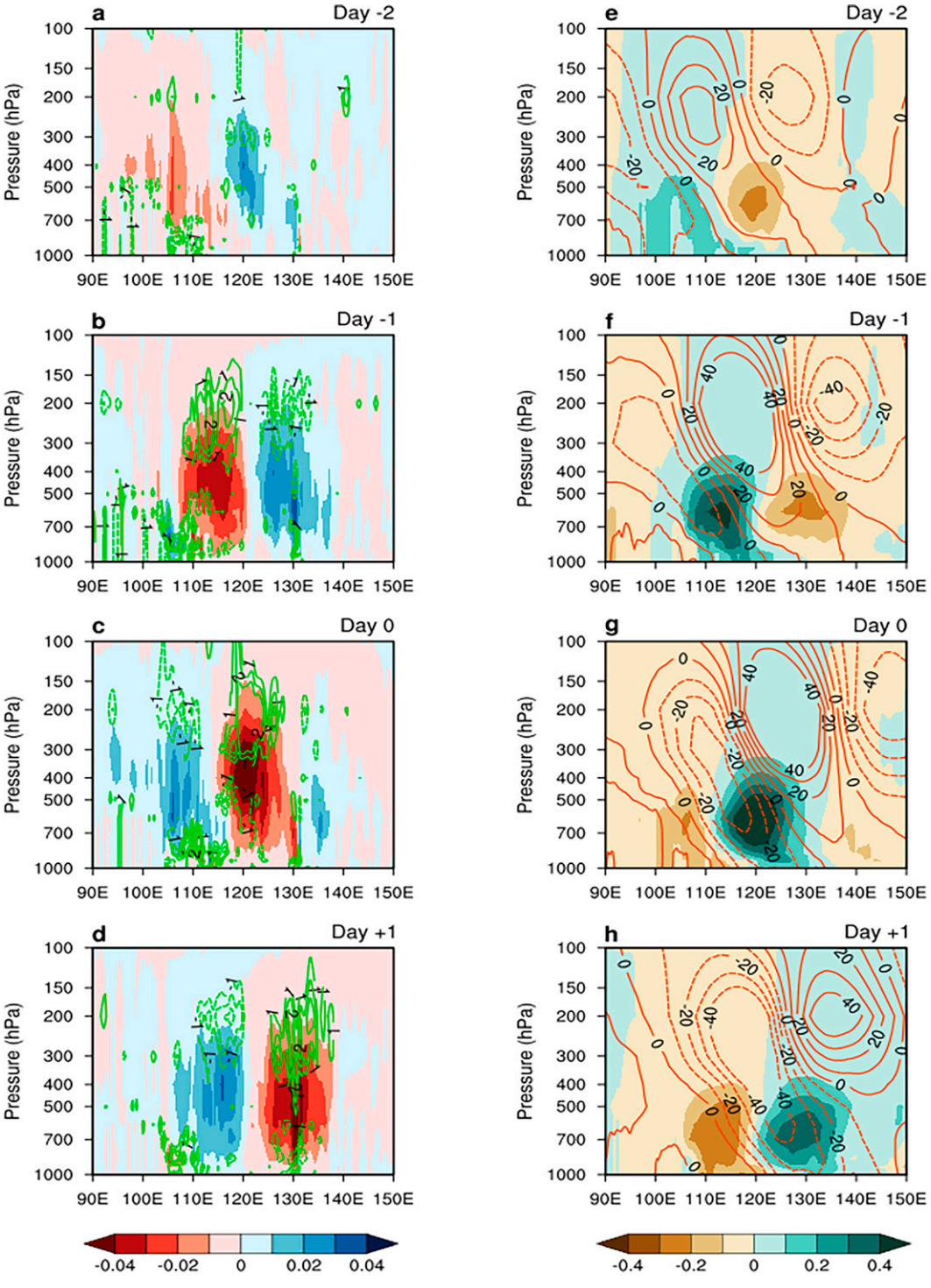

FIG. 3. (a)–(d) Zonal–vertical cross sections of synoptic-scale vertical velocity (shading; Pa s^{-1}) and divergence (contour; 10^{-6} s^{-1}, major contour levels: −2, −1, 1, and 2, with contour level 0 omitted) fields along 32°N from the ERA5 reanalysis. (e)–(h) As in (a)–(d), but for synoptic-scale specific humidity (shading; g kg^{-1}) and geopotential (contour; m^2 s^{-2}) fields. Positive contours are represented by solid lines, and negative contours are dashed.

$$\left(\frac{\partial\omega}{\partial p}\right)_3 \approx \frac{\omega_4 - \omega_2}{\delta p}.$$

The vorticity Eq. (1) can be written at levels 1 and 3 as

$$\frac{\partial}{\partial t}\nabla^2\psi_1 + V_1 \cdot \nabla(\nabla^2\psi_1) + \beta\frac{\partial\psi_1}{\partial x} = \frac{f_0}{\delta p}\omega_2, \tag{4}$$

$$\frac{\partial}{\partial t}\nabla^2\psi_3 + V_3 \cdot \nabla(\nabla^2\psi_3) + \beta\frac{\partial\psi_3}{\partial x} = \frac{f_0}{\delta p}(\omega_4 - \omega_2), \tag{5}$$

where δp is the pressure interval between levels 1 and 3 (or between levels 0 and 2), and the subscript notation is used to designate the vertical level.

We evaluate $\partial\psi/\delta p$ at level 2 using the following formula:

$$\left(\frac{\partial\psi}{\partial p}\right)_2 \approx \frac{\psi_3 - \psi_1}{\delta p}.$$

Thus, the thermodynamic Eq. (2) can then be expressed at level 2 as

$$\frac{\partial}{\partial t}(\psi_1 - \psi_3) = -V_2 \cdot \nabla(\psi_1 - \psi_3) + \frac{\delta p\sigma}{f_0}\omega_2 + \frac{\delta p\kappa\dot{Q}}{f_0 p}. \tag{6}$$

Consider a simple vertical shear background flow with a horizontally uniform zonal wind field; the perturbation streamfunction and vertical velocity fields may be expressed as

$$\begin{aligned}\psi_1 &= -U_1 y + \psi_1'(x,t),\\ \psi_3 &= -U_3 y + \psi_3'(x,t),\\ \omega_2 &= \omega_2'(x,t),\\ \omega_4 &= \omega_4'(x,t),\end{aligned} \tag{7}$$

where U_1 and U_3 are constant zonal velocities at levels 1 and 3, respectively.

Substituting Eq. (7) into Eqs. (4), (5), and (6), one may derive a set of linearized governing equations:

$$\left(\frac{\partial}{\partial t} + U_1\frac{\partial}{\partial x}\right)\frac{\partial^2\psi_1'}{\partial x^2} + \beta\frac{\partial\psi_1'}{\partial x} = \frac{f_0}{\delta p}\omega_2', \tag{8}$$

$$\left(\frac{\partial}{\partial t} + U_3\frac{\partial}{\partial x}\right)\frac{\partial^2\psi_3'}{\partial x^2} + \beta\frac{\partial\psi_3'}{\partial x} = \frac{f_0}{\delta p}(\omega_4' - \omega_2'), \tag{9}$$

$$\left(\frac{\partial}{\partial t} + U_m\frac{\partial}{\partial x}\right)(\psi_1' - \psi_3') - U_T\frac{\partial}{\partial x}(\psi_1' + \psi_3') = \frac{\delta p\sigma}{f_0}\omega_2' + \frac{\delta p\kappa\dot{Q}'}{f_0 p}. \tag{10}$$

In a modified Betts–Miller scheme, the precipitation anomalies are proportional to anomalies in column-integrated or low-level specific humidity (Wang and Chen 2017; Liu and Wang 2017; Adames and Ming 2018). Such a moisture–precipitation in-phase relation was confirmed by a number of previous observational studies (e.g., Bretherton et al. 2004; Jiang et al. 2015; Wang et al. 2017) as well as the observational analysis in this study (e.g., Figs. 2, 3). An examination of the relationship between summertime synoptic-scale moisture and precipitation fields in the mei-yu front region shows a robust and significant linear relationship between them. Therefore, the perturbation precipitation may be expressed as a function of perturbation specific humidity:

$$\mathrm{Pr}' = \frac{q_3'}{\tau}. \tag{11}$$

Note that as perturbation diabatic heating depends on the perturbation precipitation, it can be expressed as

$$\dot{Q}' = \frac{10^3 c_p}{0.26}\mathrm{Pr}'. \tag{12}$$

One may write the following formula for the perturbation diabatic heating:

$$\dot{Q}' = aq_3', \tag{13}$$

where $a = 10^3 c_p/(0.26\tau)$, and τ represents the convective adjustment time.

By defining

$$U_m \equiv (U_1 + U_3)/2,$$

$$U_T \equiv (U_1 - U_3)/2,$$

Eqs. (8) and (9) can be rewritten as

$$\left[\frac{\partial}{\partial t} + (U_m + U_T)\frac{\partial}{\partial x}\right]\frac{\partial^2\psi_1'}{\partial x^2} + \beta\frac{\partial\psi_1'}{\partial x} = \frac{f_0}{\delta p}\omega_2', \tag{14}$$

$$\left[\frac{\partial}{\partial t} + (U_m - U_T)\frac{\partial}{\partial x}\right]\frac{\partial^2\psi_3'}{\partial x^2} + \beta\frac{\partial\psi_3'}{\partial x} = \frac{f_0}{\delta p}(\omega_4' - \omega_2'). \tag{15}$$

Defining the barotropic and baroclinic components of perturbation streamfunction as

$$\psi_m \equiv (\psi_1' + \psi_3')/2,$$

$$\psi_T \equiv (\psi_1' - \psi_3')/2,$$

One may add Eqs. (14) and (15) to yield

$$\left(\frac{\partial}{\partial t} + U_m\frac{\partial}{\partial x}\right)\frac{\partial^2\psi_m}{\partial x^2} + \beta\frac{\partial\psi_m}{\partial x} + U_T\frac{\partial}{\partial x}\frac{\partial^2\psi_T}{\partial x^2} + \frac{f_0\alpha}{2\delta p}\frac{\partial^2(\psi_m - \psi_T)}{\partial x^2} = 0 \tag{16}$$

and subtract Eqs. (15) from (14) to yield

$$\left(\frac{\partial}{\partial t} + U_m\frac{\partial}{\partial x}\right)\left(\frac{\partial^2\psi_T}{\partial x^2} - 2\lambda_1^2\psi_T\right) + \beta\frac{\partial\psi_T}{\partial x} + U_T\frac{\partial}{\partial x}\left(\frac{\partial^2\psi_m}{\partial x^2} + 2\lambda_1^2\psi_m\right) - \frac{f_0\alpha}{2\delta p}\frac{\partial^2(\psi_m - \psi_T)}{\partial x^2} + \lambda_1^2\frac{\delta p\kappa a}{f_0 p}q_3' = 0, \tag{17}$$

where $\lambda_1^2 = f_0^2/[\sigma(\delta p)^2]$.

To close the system, a lower-tropospheric moisture tendency equation is introduced. The moisture change rate is

determined by anomalous horizontal and vertical advection, namely,

$$\frac{\partial q_3'}{\partial t} = -U_3\frac{\partial q_3'}{\partial x} - V_3' q_m - \omega_3' q_n - \mathrm{Pr}', \tag{18}$$

where $q_m = \partial\overline{q}/\partial y$ and $q_n = \partial\overline{q}/\partial p$ denote meridional and vertical gradients of the background moisture field in the lower troposphere. The three terms on the right-hand side of the moisture tendency equation represent anomalous zonal, meridional, and vertical advection. The moisture tendency equation can be rewritten as

$$\left(\frac{\partial}{\partial t} + U_m\frac{\partial}{\partial x}\right)q_3' = -(U_m - U_T)\frac{\partial q_3'}{\partial x} + U_m\frac{\partial q_3'}{\partial x} - q_m\frac{\partial(\psi_m - \psi_T)}{\partial x} + \alpha q_n\frac{\partial^2(\psi_m - \psi_T)}{\partial x^2} - \frac{q_3'}{\tau}. \tag{19}$$

To sum up, a set of linearized governing equations for the moist baroclinic dynamics are constructed. It is a closed system with three dependent variables: barotropic and baroclinic streamfunction fields and lower-tropospheric specific humidity field. The three governing equations can be written as

$$\left(\frac{\partial}{\partial t} + U_m\frac{\partial}{\partial x}\right)\frac{\partial^2\psi_m}{\partial x^2} + \beta\frac{\partial\psi_m}{\partial x} + U_T\frac{\partial}{\partial x}\frac{\partial^2\psi_T}{\partial x^2} + \lambda_2\frac{\partial^2(\psi_m - \psi_T)}{\partial x^2} = 0, \tag{20}$$

$$\left(\frac{\partial}{\partial t} + U_m\frac{\partial}{\partial x}\right)\left(\frac{\partial^2\psi_T}{\partial x^2} - 2\lambda_1^2\psi_T\right) + \beta\frac{\partial\psi_T}{\partial x} + U_T\frac{\partial}{\partial x}\left(\frac{\partial^2\psi_m}{\partial x^2} + 2\lambda_1^2\psi_m\right) - \lambda_2\frac{\partial^2(\psi_m - \psi_T)}{\partial x^2} + \lambda_1^2\lambda_3 q_3' = 0, \tag{21}$$

$$\left(\frac{\partial}{\partial t} + U_m\frac{\partial}{\partial x}\right)q_3' = -(U_m - U_T)\frac{\partial q_3'}{\partial x} + U_m\frac{\partial q_3'}{\partial x} - \lambda_4\frac{\partial(\psi_m - \psi_T)}{\partial x} + \lambda_5\frac{\partial^2(\psi_m - \psi_T)}{\partial x^2} - \frac{q_3'}{\tau}, \tag{22}$$

where $\lambda_1^2 = f_0^2/[\sigma(\delta p)^2]$, $\lambda_2 = \alpha f_0/(2\delta p)$, $\lambda_3 = \kappa a\delta p/(f_0 p)$, $\lambda_4 = q_m$, and $\lambda_5 = \alpha q_n$.

5. Eigenvalue solutions and phase structures of the most unstable mode

Let us consider wavelike solutions for Eqs. (20)–(22) with the following forms:

$$\psi_m = Ae^{ik(x-ct)},$$

$$\psi_T = Be^{ik(x-ct)},$$

$$q_3' = Ce^{ik(x-ct)},$$

where A, B, and C represent the amplitude, k denotes the zonal wavenumber, $i = (-1)^{1/2}$ is the imaginary unit, and c designates the phase speed.

TABLE 2. Parameters used in the moist baroclinic model.

Angular speed of rotation of the Earth	$\Omega = 7.292 \times 10^{-9}$ rad s^{-1}
Radius of the Earth	$R_E = 6.37 \times 10^6$ m
Reference latitude	$\varphi = 30°$N
Gas constant for dry air	$R = 287$ J K^{-1} kg^{-1}
Specific heat of dry air at constant pressure	$c_p = 1004$ J K^{-1} kg^{-1}
Ratio of gas constant to specific heat at constant pressure	$\kappa = 0.286$
Latent heat of vaporization	$L_v = 2.5 \times 10^6$ J kg^{-1}
Density scale height	$H = 8000$ m
Pressure interval between level 1 and 3	$\delta p = 40\,000$ Pa
Mean zonal velocity at level 1	$U_1 = 20$ m s^{-1}
Mean zonal velocity at level 3	$U_3 = 5$ m s^{-1}
Mean meridional gradient of specific humidity	$q_m = 4 \times 10^{-9}$ kg kg^{-1} m^{-1}
Mean vertical gradient of specific humidity	$q_n = 3 \times 10^{-7}$ kg kg^{-1} Pa^{-1}
Eddy viscosity coefficient	$K_m = 10$ m^2 s^{-1}
Static stability parameter	$\sigma = 2 \times 10^{-6}$ m^2 Pa^{-2} s^{-2}
Convective adjustment time	$\tau = 2$ days

Substituting these solutions into Eqs. (20), (21), and (22) yields

$$[i(c - U_m)k^2 + i\beta - \lambda_2 k]A - (ik^2U_T - \lambda_2 k)B = 0, \tag{23a}$$

$$[iU_T(-k^3 + 2\lambda_1^2 k) + \lambda_2 k^2]A + [i(c - U_m)(k^3 + 2\lambda_1^2 k) + i\beta k - \lambda_2 k^2]B + \lambda_1^2\lambda_3 C = 0, \tag{23b}$$

$$(\lambda_5 k^2 + \lambda_4 ik)A - (\lambda_5 k^2 + \lambda_4 ik)B + [-i(c - U_m)k + (U_m - U_T)ik - U_m ik + \tau^{-1}]C = 0. \tag{23c}$$

To obtain a set of nonzero solutions, the coefficient determinant of Eqs. (23a)–(23c) must vanish. Through a series of derivation, the final dispersion equations for the real and imaginary parts of c (i.e., c_r and c_i) can be written as

$$\varepsilon_1 c_r^3 - 3\varepsilon_1 c_r c_i^2 - \varepsilon_2 c_r^2 + \varepsilon_2 c_i^2 - 2\varepsilon_3 c_r c_i + \varepsilon_4 c_r + \varepsilon_5 c_i + \varepsilon_6 = 0, \tag{24a}$$

$$\varepsilon_1 c_i^3 - 3\varepsilon_1 c_r^2 c_i - \varepsilon_3 c_r^2 + \varepsilon_3 c_i^2 + 2\varepsilon_2 c_r c_i + \varepsilon_5 c_r - \varepsilon_4 c_i + \varepsilon_7 = 0, \tag{24b}$$

where ε_1, ε_2, …, and ε_7 are the function of the background mean state and zonal wavenumber k (see the appendix).

Newton's iterative method can be used to solve the dispersion equations. The control parameters in the moist baroclinic model such as the basic state upper- and lower-tropospheric zonal wind speed ($U_1 = 20$ m s^{-1} and $U_3 = 5$ m s^{-1}), basic state meridional and vertical moisture gradients, and eddy viscosity coefficient are listed in Table 2.

Figure 4 shows the results of eigenvalue analysis with the use of a set of control parameters. Here, the growth rate kc_i and phase speed c_r are given as a function of zonal wavenumber k.

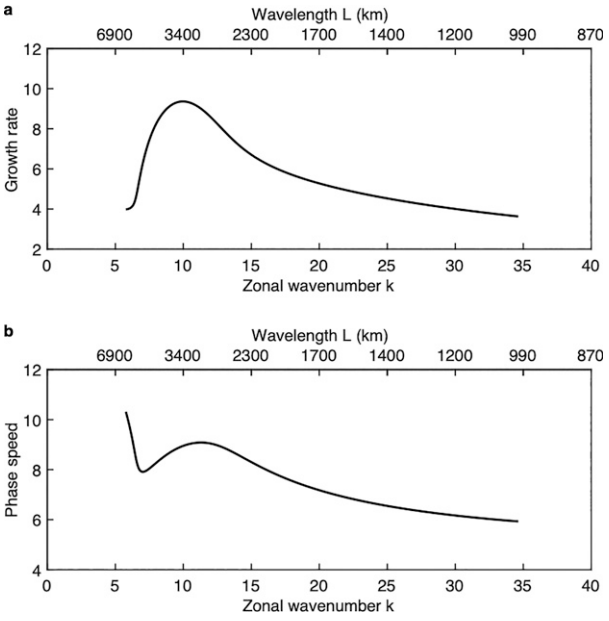

FIG. 4. (a) Growth rate (10^{-6} s^{-1}) and (b) phase speed (m s^{-1}) as a function of zonal wavenumber from the moist baroclinic model.

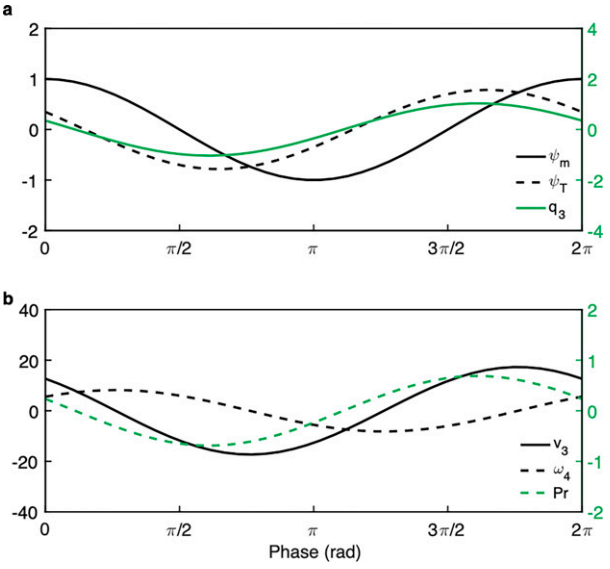

FIG. 5. Zonal phase relations among (a) barotropic streamfunction ψ_m (10^7 m^2 s^{-1}), baroclinic streamfunction ψ_T (10^7 m^2 s^{-1}), and lower-tropospheric specific humidity q_3 (g kg^{-1}); (b) lower-level meridional wind v_3 (m s^{-1}), vertical velocity at the top of PBL ω_4 (10^{-3} Pa s^{-1}), and precipitation Pr (mm day^{-1}) for the most unstable mode.

It is interesting to note that the growth rate peaks at wavenumber 10, corresponding to a zonal wavelength of 3400 km, which is in good agreement with the observational analysis result shown in section 3. Similar to the classic baroclinic instability theory, the most unstable mode prefers an intermediate scale, while both very long and short length scales are not favorable. The maximum growth rate is 9.36×10^{-6} s^{-1} (Fig. 4a), which is equivalent to an *e*-folding scale of about one day, favorable for the development of synoptic-scale disturbances. The zonal-phase speed of the most unstable mode is about 9 m s^{-1} (Fig. 4b). Again, this is in good agreement with observations.

The zonal phase structures and phase relations among various key variables for the most unstable mode are illustrated in Fig. 5. The baroclinic streamfunction ψ_T lags the barotropic streamfunction ψ_3 by about 90°, and the amplitude of ψ_3 appears larger than that of ψ_T (Fig. 5a). While the specific humidity and precipitation fields are zonally in phase, they are slightly behind ψ_T. A prominent feature is the phase relation among lower-tropospheric meridional wind v_3, vertical velocity at the top of PBL ω_4, and lower-tropospheric specific humidity q_3. The peak of q_3 is somewhere between the maximum phase of v_3 and the minimum phase of ω_4. This implies that both anomalous lower-tropospheric meridional moisture advection (i.e., northward advection of high background-mean moisture by anomalous southerlies) and vertical moisture advection by Ekman pumping–induced anomalous ascending motion contribute to the lower-level moistening, which further strengthens the perturbation development through condensational heating.

The tilting vertical structure of the most unstable mode may be better described by the upper- and lower-tropospheric streamfunction fields (Fig. 6a). As seen in Fig. 6a, the upper-tropospheric streamfunction ψ_1 lags the lower-tropospheric streamfunction ψ_3 by about 90°, while the amplitude of ψ_1 is larger than that of ψ_3. This indicates a westward-tilting vertical structure, with a trough at 250 hPa about 90° in phase behind a trough at 750 hPa. Both a greater amplitude of ψ_1 in

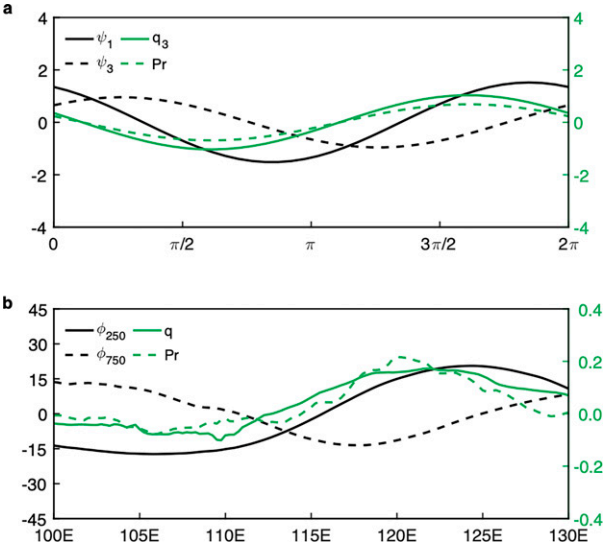

FIG. 6. (a) Zonal-phase relations among upper-tropospheric streamfunction ψ_1 (10^7 m^2 s^{-1}), lower-tropospheric streamfunction ψ_3 (10^7 m^2 s^{-1}), q_3 (g kg^{-1}), and Pr (mm day^{-1}) for the most unstable mode in the moist baroclinic model. (b) Observed counterparts for synoptic-scale motions: geopotential height at 250 hPa ϕ_{250} (m^2 s^{-2}), geopotential height at 750 hPa ϕ_{750} (m^2 s^{-2}), specific humidity at 850 hPa q (g kg^{-1}), and precipitation Pr (mm day^{-1}) along 32°N from the ERA5 reanalysis.

the upper troposphere and the westward-tilting vertical structure are consistent with the observed synoptic-scale disturbances (Fig. 3e–h). The peak phases of q_3 and Pr are located east of the lower-level trough because the trough induces local ascending motion at the top of PBL and anomalous southerly winds east of the trough, both of which contribute to atmospheric moistening.

The observed phase relations among synoptic-scale 250- and 750-hPa geopotential height, 750-hPa specific humidity, and precipitation fields along 32°N on day 0 are shown in Fig. 6b. The upper-tropospheric geopotential height ϕ_{250} lags the lower-tropospheric counterpart ϕ_{750} in a way similar to that in Fig. 6a, and the amplitude of ϕ_{250} is larger than that of ϕ_{750}. The upper-level trough lies about 90° in phase west of the lower-level trough, and the trough and ridge axes show a westward tilt with height. The maximum precipitation and specific humidity anomalies appear slightly east of the lower-tropospheric trough axis. All these observed features are well reproduced by the moist baroclinic model.

The eigenvalue analysis of the simple theoretical model indicates that in the presence of the moisture–convection–circulation feedback, the most unstable mode under a finite background vertical shear over the subtropical mei-yu front has a preferred synoptic-scale wavelength of about 3400 km and a tilted vertical structure. The circulation is tightly coupled with the moisture and precipitation fields, with maximum moisture and precipitation anomalies slightly leading the lower-level trough. The most unstable disturbance propagates eastward at a phase speed of about 9 m s^{-1}. These features are in good agreement with those of the observed synoptic-scale perturbations, suggesting that the moist baroclinic instability theory proposed in this study is capable of explaining the observed characteristics of synoptic-scale disturbances along the mei-yu front.

6. Sensitivity of the model solution to key parameters

In this section, we assess the sensitivity of the moist baroclinic model solution to some key parameters such as the diabatic heating coefficient a (or the convective adjustment time τ) and the background vertical shear. These parameters are crucial for the perturbation growth of synoptic-scale disturbances along the mei-yu front.

The first parameter to test is the diabatic heating coefficient, as latent heat is an important energy source for the development of synoptic-scale disturbances along the mei-yu front. Similar to polar and midlatitude fronts, mei-yu fronts are associated with strong diabatic heating due to the formation of frontal clouds and heavy rainfall that may provide effective feedbacks to the frontal circulation (Hu et al. 2021). The diabatic heating due to increased moisture drives a dynamical response in large-scale circulation and vertical motion (Nie et al. 2018). To examine the sensitivity of the strength of diabatic heating in modulating the growth and structure of the unstable mode, we choose different convective adjustment times with τ specified to be 0.5, 1.0, and 2.0 days.

Figure 7 shows the model solutions with different convective adjustment times. As the convective adjustment time τ decreases, the growth rate of the most unstable mode increases, while the wavelength of the most unstable mode is reduced. The amplitudes of ψ_1 and ψ_3 become larger, with the precipitation amount increasing east of the lower-tropospheric trough.

The fact that maximum precipitation (or diabatic heating) center is located somewhere between the lower-tropospheric trough and upper-tropospheric ridge is critical for perturbation growth. This is because on the one hand the positive heating anomalies increase midtropospheric temperature and thus deepens both the lower-level trough and the upper-level ridge, and on the other hand the strengthened lower-level trough further increases the moisture and thus diabatic heating through enhanced northward and Ekman pumping–induced upward moisture advection. The smaller the convective adjustment time τ is, the greater the diabatic heating becomes, and the stronger the amplification of the synoptic-scale disturbances will be.

The background vertical shear associated with meridional temperature gradient is critical for the perturbation growth in the classic baroclinic instability theory. How does the background vertical shear impact the subtropical front in boreal summer? The second parameter we examine is the strength of the background vertical shear. Three sets of the mean zonal velocities at levels 1 and 3 are specified: $U_1 = 15$ m s^{-1}, $U_3 = 5$ m s^{-1}; $U_1 = 20$ m s^{-1}, $U_3 = 5$ m s^{-1}; and $U_1 = 25$ m s^{-1}, $U_3 = 5$ m s^{-1}. With the increase of the vertical shear, the growth rate of the most unstable mode increases as expected. An interesting feature is the shift of the wavelength from short to long (i.e., from wavenumber 12 to 6) for the most unstable mode as the vertical shear increases (Fig. 8a).

While the growth rate shows a marked change with the aforementioned vertical shear change, the amplitude and phase structure of the upper- and lower-tropospheric streamfunction fields ψ_1 and ψ_3 exhibit less sensitivity (Figs. 8b,c). The precipitation anomalies tend to be stronger under a weaker background vertical shear as the lower-level trough axis is closer to the upper-level ridge axis (Fig. 8d).

Would instability still occur in the absence of background vertical shear? To address this question, we conducted an additional test without the background vertical shear ($U_1 = 5$ m s^{-1}, $U_3 = 5$ m s^{-1}). It is found that in the absence of vertical shear, instability still occurs (Fig. 9a). This demonstrates the critical role of the moisture–convection feedback in generating instability. Note that in this case the upper-level and lower-level streamfunction anomalies have an opposite phase, and the maximum precipitation and moisture anomalies are located east of the lower-level trough (Fig. 9c) due to the combined effect of the anomalous horizontal and vertical advection. As in the control case (Fig. 4a), the most unstable mode has a preferred zonal wavelength of about 3400 km, even though the growth rate is reduced a little due to the lack of background vertical shear (Fig. 9a). The zonal phase speed of the most unstable mode in this case is about 7 m s^{-1} (Fig. 9b), which is slightly greater than the column-averaged zonal mean flow.

What happens if the moisture and precipitation are completely decoupled with the circulation? A further sensitivity test is carried out with the precipitation and moisture anomalies kept zero (Figs. 9d–f). This case returns to the classic baroclinic instability

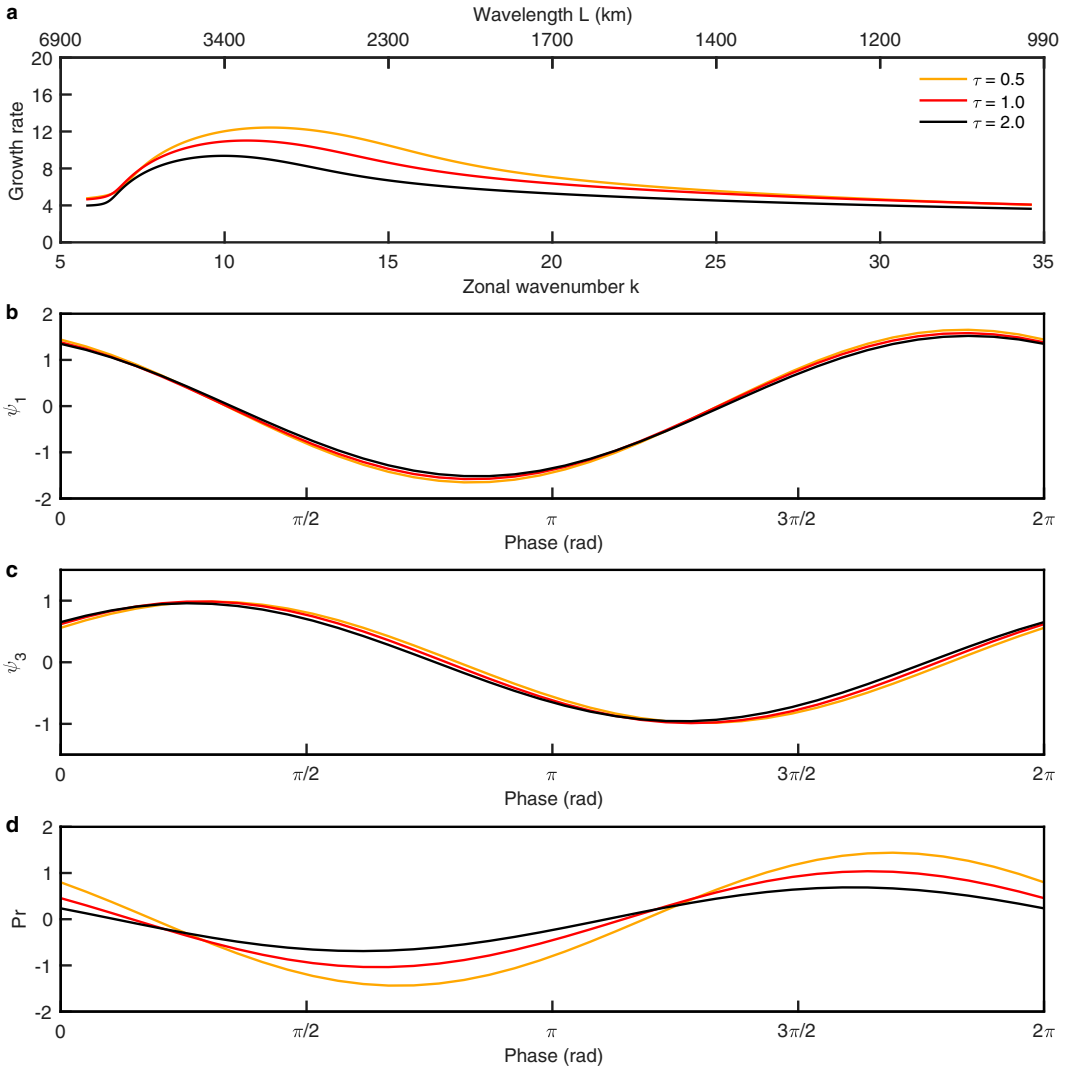

FIG. 7. The sensitivity tests of (a) dependence of the growth rate (10^{-6} s^{-1}) and the zonal-phase relations among (b) ψ_1 (10^7 m^2 s^{-1}), (c) ψ_3 (10^7 m^2 s^{-1}), and (d) Pr (mm day^{-1}) for the most unstable mode on the convective adjustment time τ.

framework. As expected, a background vertical shear with the value in Table 1 can cause an instability, but the growth rate becomes much weaker compared to that shown in Fig. 4a in the presence of the moisture–convection–circulation feedback. Note that the preferred zonal wavelength of the most unstable mode in this case is much larger (about 4500 km), resembling that derived from the classic baroclinic instability model (Holton 2004).

Figure 10 shows additional sensitivity test results with respect to the background meridional moisture gradient and the Ekman layer. The meridional moisture gradient is set to zero, reduced by 50%, and increased by 50%. Both the growth rate and eastward phase speed increase as the background moisture gradient strengthens, which is consistent with the result of Sobel et al. (2001). When the background meridional moisture gradient is set to be zero, the instability still occurs, which is primarily caused by Ekman pumping–induced vertical moisture advection. There is a slight increase in the wavelength of the most unstable mode in this case.

Finally, consider a special case in the absence of the Ekman layer. As illustrated in Fig. 10, When the Ekman layer is neglected in the midlatitude synoptic-scale systems, the growth rate of the most unstable mode decreases slightly compared to the control case (Fig. 4). This suggests that the Ekman process is not critical in generating the moist baroclinic instability over the mei-yu front.

7. Summary and discussion

We constructed a simple theoretical model to understand the most unstable mode along the subtropical mei-yu front. A unique feature of disturbances along the subtropical front is

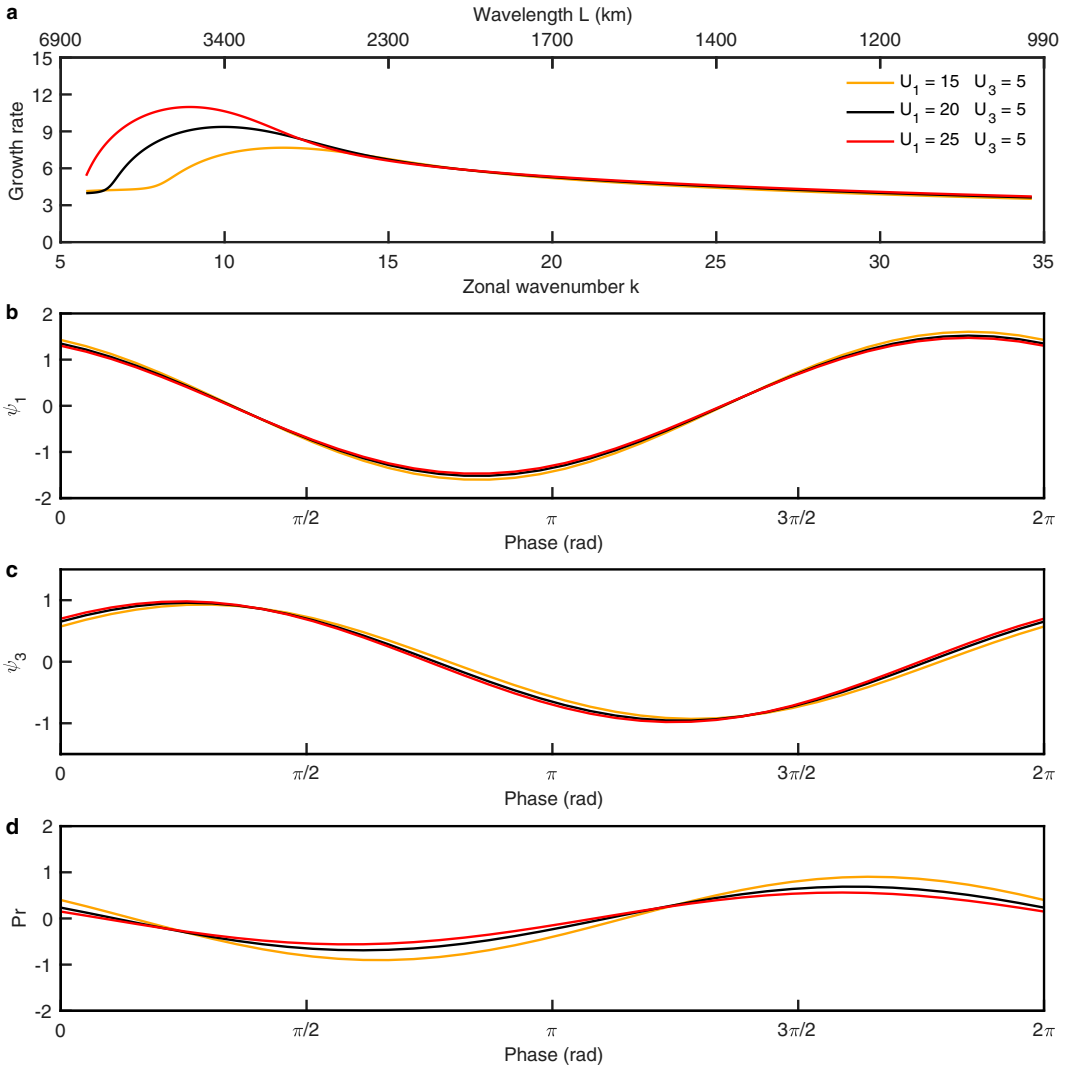

FIG. 8. The sensitivity tests of (a) dependence of the growth rate (10^{-6} s^{-1}) and the zonal phase relations among (b) ψ_1 (10^7 m^2 s^{-1}), (c) ψ_3 (10^7 m^2 s^{-1}), and (d) Pr (mm day^{-1}) for the most unstable mode on the background vertical shear.

the coupling of moisture and precipitation processes to free-atmospheric circulation under a moderate vertical shear. This differs markedly from the classic dry baroclinic instability framework.

An observational analysis shows that the dominant signal along the subtropical mei-yu front is synoptic-scale perturbations that propagate eastward over the Yangtze River valley in eastern China. The precipitation anomalies associated with the synoptic-scale disturbances are northeast–southwest oriented, with a clear baroclinic vertical structure in the wind fields and a westward tilt with height in the geopotential height fields. The maximum moisture and precipitation anomalies are located slightly east of the lower-tropospheric cyclonic center. The observed synoptic-scale disturbances along the mei-yu front have a typical wavelength of about 3400 km.

The moist baroclinic instability model is an extension of the classic two-level baroclinic instability model of Phillips (1954). In addition to quasigeostrophic vorticity and thermodynamic equations, we consider a lower-tropospheric moisture tendency equation that consists of three-dimensional moisture advection processes. A modified Betts–Miller scheme is used to link the perturbation precipitation and moisture fields. A well-mixed PBL is included to mimic the Ekman pumping–induced vertical velocity at the top of PBL. An iterative method is used to find the solutions of the dispersion equations.

The results of eigenvalue analysis show that in a realistic parameter regime, the model favors the most unstable mode with a maximum growth rate at zonal wavenumber 10, corresponding to a zonal wavelength of 3400 km, and a phase speed of about 9 m s^{-1}. The maximum growth rate is

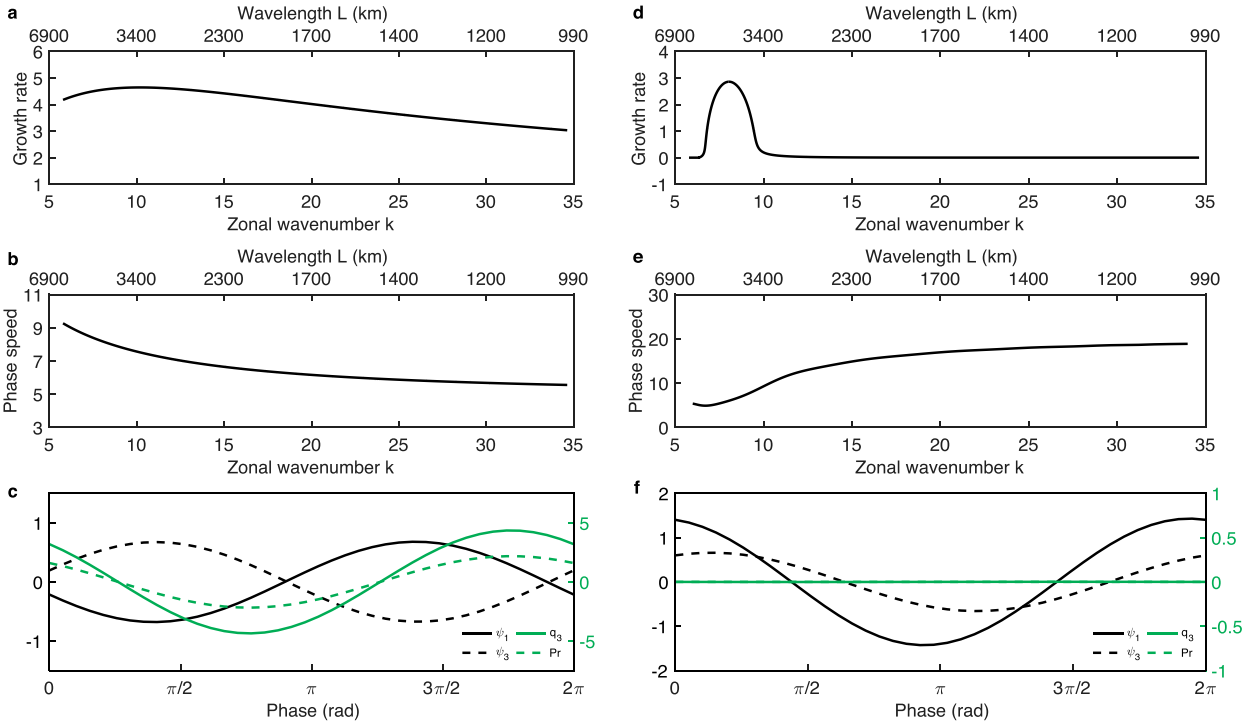

FIG. 9. (a) Growth rate (10^{-6} s^{-1}) and (b) phase speed (m s^{-1}) as a function of zonal wavenumber in the simple analytical model without vertical shear. (c) Zonal-phase relations among upper-tropospheric streamfunction ψ_1 (10^7 m^2 s^{-1}), lower-tropospheric streamfunction ψ_3 (10^7 m^2 s^{-1}), q_3 (g kg^{-1}), and Pr (mm day^{-1}) for the most unstable mode in the absence of the vertical shear. (d) Growth rate (10^{-6} s^{-1}) and (e) phase speed (m s^{-1}) as a function of zonal wavenumber in the simple analytical model without diabatic heating. (f) Zonal-phase relations among upper-tropospheric streamfunction ψ_1 (10^7 m^2 s^{-1}), lower-tropospheric streamfunction ψ_3 (10^7 m^2 s^{-1}), q_3 (g kg^{-1}), and Pr (mm day^{-1}) for the most unstable mode in the absence of the diabatic heating.

9.36×10^{-6} s^{-1}, which is equivalent to an *e*-folding scale of 1 day. The most unstable mode has a westward-tilted baroclinic structure, with upper-tropospheric streamfunction ψ_1 lagging the lower-tropospheric streamfunction ψ_3 by about 90°. The amplitude of the upper-tropospheric streamfunction is in general greater than that of its lower-tropospheric counterpart. The maximum lower-tropospheric moisture and precipitation anomalies located slightly east of the lower-tropospheric trough are zonally in phase. Such a phase relation implies that the lower-level specific humidity is primarily determined by anomalous meridional advection by southerly winds in front of the trough and anomalous vertical advection associated with the Ekman pumping–induced ascent over the trough. The results indicate that the moist baroclinic instability model captures well the observed characteristics of synoptic-scale disturbances over the mei-yu front.

The sensitivity of the model solution to some key parameters is further examined. We found that the diabatic heating associated with the moisture–precipitation–circulation feedback dominates the instability, and it is a primary source for the destabilization of synoptic-scale disturbances over the mei-yu front. The background vertical shear also contributes to the instability, and it is critical to the formation of the tilted vertical structure. Thus, the vertical shear provides an additional energy source for the growth of synoptic-scale perturbations along the mei-yu front. The zonal-scale selection is primarily determined by the moisture–convection–circulation feedback. It has been demonstrated that under zero vertical shear, the zonal wavelength of the most unstable mode remains the same as in the control case in the presence of vertical shear. As the background moisture gradient strengthens, the growth rate and eastward phase speed increase. There is evidence that the Ekman layer is not essential in generating the moist baroclinic instability along the mei-yu front.

While this moist baroclinic dynamic model is a useful tool for understanding the summertime wave development along the subtropical mei-yu front, its framework involves a number of assumptions and has its own limitations. For instance, a horizontally uniform background zonal mean flow is assumed, and the perturbation diabatic heating is proportional to the low-level perturbation moisture. In the original Betts–Miller scheme, the precipitation depends on both moisture and temperature. We intend to include temperature dependence in the convective parameterization scheme in future studies. In addition, cold pools may impact the divergence and vorticity around the convective systems. This framework does not consider the role of cold pool–related circulation in changing the horizontal and vertical moisture advection.

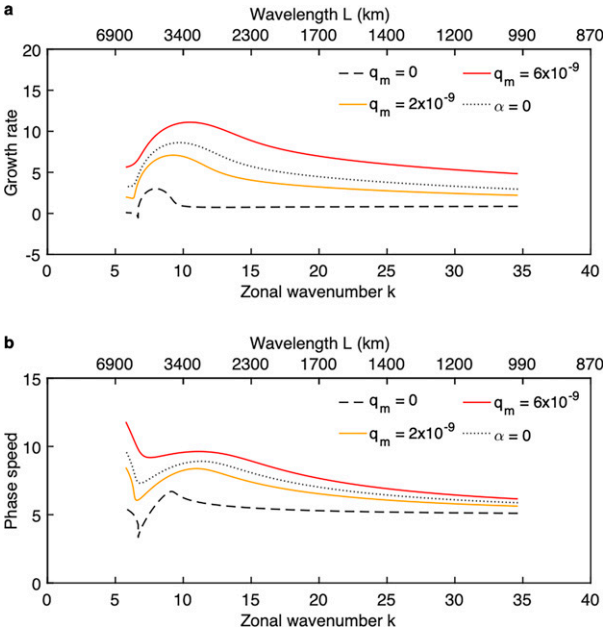

FIG. 10. (a) Growth rate (10^{-6} s^{-1}) and (b) phase speed (m s^{-1}) as a function of zonal wavenumber in the simple analytical model when the background meridional moisture gradient (kg kg^{-1} m^{-1}) is set to zero (dashed line), decreased by 50% (orange line), increased by 50% (red line), and in the absence of the Ekman layer (dotted line).

It is worth mentioning that this moist baroclinic instability framework differs from a tropics-oriented instability framework in which a weak temperature gradient (WTG) approximation was applied (e.g., Adames and Ming 2018). According to the thermal wind relation, the WTG implies a weak vertical shear, and to the first order of approximation the diabatic heating under the WTG is balanced by the adiabatic process associated with vertical motion. In contrast, this framework incorporates advective processes associated with the meridional moisture gradient and the vertical shear in the subtropics. The common process included in both frameworks is the lower-tropospheric moistening associated with diabatic heating.

A further study with a specified three-dimensional background mean flow in the multilevel general circulation model may be conducted, following the strategy applied in Li (2006). A regional or global climate model with a sophisticated convective parameterization scheme may be utilized to tackle this problem. For instance, one may specify the observed climatological summer mean flow and a synoptic-scale perturbation as an initial condition in a control experiment, and then subtract the control simulation from a parallel simulation with the climatological mean flow only. By examining the difference between the two experiments, one may reveal the role of the background mean flow on the perturbation growth (Zhao and Li 2019). The results from the aforementioned, more sophisticated models may be compared with those from the moist baroclinic model to show the similarities and contrasts due to the complexity of the models. As synoptic-scale disturbances in the East Asian summer monsoon region have profound impacts on the tropical and subtropical weather and climate, further studies on projected changes of synoptic-scale variability along the subtropical mei-yu front under global warming are urgently needed.

Acknowledgments. This work was jointly supported by NSFC Grant 42088101, NOAA NA18OAR4310298, and NSF AGS-2006553.

Data availability statement. The Global Precipitation Climatology Project data are available from https://www.ncdc.noaa.gov/wdcmet/data-access-search-viewer-tools/global-precipitation-climatology-project-gpcp-clearinghouse. The ERA5 reanalysis data were downloaded from https://climate.copernicus.eu/climate-reanalysis.

APPENDIX

Derivation from Eqs. (23) to Eqs. (24)

To obtain nonzero solutions for Eqs. (23a)–(23c), the coefficient determinant must be zero. Therefore, we have

$$\begin{vmatrix} i[(c-U_m)k^2+\beta]-\lambda_2 k & -ik^2U_T+\lambda_2 k & 0 \\ iU_T(-k^3+2\lambda_1^2 k)+\lambda_2 k^2 & i(c-U_m)(k^3+2\lambda_1^2 k) & \lambda_1^2\lambda_3 \\ & +i\beta k-\lambda_2 k^2 & \\ \lambda_5 k^2+\lambda_4 ik & -\lambda_5 k^2-\lambda_4 ik & -i(c-U_m)k+i(U_m-U_T)k \\ & & -iU_m k+\tau^{-1} \end{vmatrix} = 0.$$

This leads to the following dispersion equation:

$$
\begin{aligned}
&ic^3(2\lambda_1^2k^4+k^6)-ic^2[(U_m-U_T)(2\lambda_1^2k^4+k^6)-2U_m(2\lambda_1^2k^4+k^6)+2\beta(\lambda_1^2k^2+k^4)]\\
&+ic\begin{bmatrix}2U_m(U_m-U_T)(2\lambda_1^2k^4+k^6)-2(U_m-U_T)\beta(\lambda_1^2k^2+k^4)+U_m^2(2\lambda_1^2k^4+k^6)\\+U_T^2(2\lambda_1^2k^4-k^6)-2U_m\beta(\lambda_1^2k^2+k^4)+\beta^2k^2+\lambda_1^2\lambda_3\lambda_5k^4-2(\lambda_2k^4+\lambda_1^2\lambda_2k^2)\tau^{-1}\end{bmatrix}\\
&-c^2[(2\lambda_1^2\lambda_2k^3+2\lambda_2k^5)+(k^5+2\lambda_1^2k^3)\tau^{-1}]\\
&+c\begin{bmatrix}(U_m-U_T)(2\lambda_1^2\lambda_2k^3+2\lambda_2k^5)+U_m(2\lambda_1^2\lambda_2k^3+2\lambda_2k^5)-U_T(2\lambda_1^2\lambda_2k^3-2\lambda_2k^5)\\-2\beta\lambda_2k^3-\lambda_1^2\lambda_3\lambda_4k^3+U_m(2k^5+4\lambda_1^2k^3)\tau^{-1}-\beta(2k^3+2\lambda_1^2k)\tau^{-1}\end{bmatrix}\\
&-iU_m^2(U_m-U_T)(2\lambda_1^2k^4+k^6)-iU_T^2(U_m-U_T)(2\lambda_1^2k^4-k^6)\\
&+iU_m(U_m-U_T)\beta(2\lambda_1^2k^2+2k^4)-i(U_m-U_T)\beta^2k^2\\
&-iU_m\lambda_1^2\lambda_3\lambda_5k^4-iU_T\lambda_1^2\lambda_3\lambda_5k^4+i\beta\lambda_1^2\lambda_3\lambda_5k^2\\
&+iU_m(2\lambda_2k^4+2\lambda_1^2\lambda_2k^2)\tau^{-1}+iU_T(2\lambda_2k^4-2\lambda_1^2\lambda_2k^2)\tau^{-1}-2i\beta\lambda_2k^2\tau^{-1}\\
&-U_m(U_m-U_T)(2\lambda_1^2\lambda_2k^3+2\lambda_2k^5)+U_T(U_m-U_T)(2\lambda_1^2\lambda_2k^3-2\lambda_2k^5)\\
&+2(U_m-U_T)\beta\lambda_2k^3+U_m\lambda_1^2\lambda_3\lambda_4k^3+U_T\lambda_1^2\lambda_3\lambda_4k^3-\beta\lambda_1^2\lambda_3\lambda_4k\\
&-U_m^2(k^5+2\lambda_1^2k^3)\tau^{-1}+U_T^2(k^5-2\lambda_1^2k^3)\tau^{-1}+U_m\beta(2k^3+2\lambda_1^2k)\tau^{-1}-\beta^2k\tau^{-1}\\
&=0.
\end{aligned}
$$

Assume that the complex phase speed has the following form:

$$c=c_r+ic_i,$$

where c_r and c_i are the real and imaginary parts of c, respectively. Thus, the above dispersion equation may be rewritten in term of c_r and c_i as

$$
\begin{aligned}
&\left\{\begin{aligned}
&(c_r^3-3c_rc_i^2)(2\lambda_1^2k^4+k^6)\\
&-c_r^2[(U_m-U_T)(2\lambda_1^2k^4+k^6)+U_m(4\lambda_1^2k^4+2k^6)-(2\beta\lambda_1^2k^2+2\beta k^4)]\\
&+c_i^2[(U_m-U_T)(2\lambda_1^2k^4+k^6)+U_m(4\lambda_1^2k^4+2k^6)-(2\beta\lambda_1^2k^2+2\beta k^4)]\\
&-c_rc_i[(4\lambda_1^2\lambda_2k^3+4\lambda_2k^5)+(2k^5+4\lambda_1^2k^3)\tau^{-1}]\\
&+c_r\begin{bmatrix}U_m(U_m-U_T)(4\lambda_1^2k^4+2k^6)-(U_m-U_T)\beta(2\lambda_1^2k^2+2k^4)\\+U_m^2(2\lambda_1^2k^4+k^6)+U_T^2(2\lambda_1^2k^4-k^6)-U_m\beta(2\lambda_1^2k^2+2k^4)\\+\beta^2k^2+\lambda_1^2\lambda_3\lambda_5k^4-(2\lambda_2k^4+2\lambda_1^2\lambda_2k^2)\tau^{-1}\end{bmatrix}\\
&+c_i\begin{bmatrix}(U_m-U_T)(2\lambda_1^2\lambda_2k^3+2\lambda_2k^5)+U_m(2\lambda_1^2\lambda_2k^3+2\lambda_2k^5)-U_T(2\lambda_1^2\lambda_2k^3-2\lambda_2k^5)\\-2\beta\lambda_2k^3-\lambda_1^2\lambda_3\lambda_4k^3+U_m(2k^5+4\lambda_1^2k^3)\tau^{-1}-\beta(2k^3+2\lambda_1^2k)\tau^{-1}\end{bmatrix}\\
&-U_m^2(U_m-U_T)(2\lambda_1^2k^4+k^6)-U_T^2(U_m-U_T)(2\lambda_1^2k^4-k^6)\\
&+U_m(U_m-U_T)\beta(2\lambda_1^2k^2+2k^4)-(U_m-U_T)\beta^2k^2\\
&-U_m\lambda_1^2\lambda_3\lambda_5k^4-U_T\lambda_1^2\lambda_3\lambda_5k^4+\beta\lambda_1^2\lambda_3\lambda_5k^2\\
&+U_m(2\lambda_2k^4+2\lambda_1^2\lambda_2k^2)\tau^{-1}+U_T(2\lambda_2k^4-2\lambda_1^2\lambda_2k^2)\tau^{-1}-2\beta\lambda_2k^2\tau^{-1}
\end{aligned}\right\}\\
&+
\end{aligned}
$$

$$
\left\{
\begin{array}{l}
(c_i^3 - 3c_r^2c_i)(2\lambda_1^2k^4 + k^6) \\
- c_r^2[(2\lambda_1^2\lambda_2k^3 + 2\lambda_2k^5) + (k^5 + 2\lambda_1^2k^3)\tau^{-1}] + c_i^2[(2\lambda_1^2\lambda_2k^3 + 2\lambda_2k^5) + (k^5 + 2\lambda_1^2k^3)\tau^{-1}] \\
+ c_rc_i[(U_m - U_T)(4\lambda_1^2k^4 + 2k^6) + U_m(8\lambda_1^2k^4 + 4k^6) - (4\beta\lambda_1^2k^2 + 4\beta k^4)] \\
+ c_r\begin{bmatrix} (U_m - U_T)(2\lambda_1^2\lambda_2k^3 + 2\lambda_2k^5) + U_m(2\lambda_1^2\lambda_2k^3 + 2\lambda_2k^5) \\ - U_T(2\lambda_1^2\lambda_2k^3 - 2\lambda_2k^5) - 2\beta\lambda_2k^3 - \lambda_1^2\lambda_3\lambda_4k^3 \\ +U_m(2k^5 + 4\lambda_1^2k^3)\tau^{-1} - \beta(2k^3 + 2\lambda_1^2k)\tau^{-1} \end{bmatrix} \\
+c_i\begin{bmatrix} (U_m - U_T)\beta(2\lambda_1^2k^2 + 2k^4) - U_m(U_m - U_T)(4\lambda_1^2k^4 + 2k^6) \\ - U_m^2(2\lambda_1^2k^4 + k^6) + U_m\beta(2\lambda_1^2k^2 + 2k^4) - U_T^2(2\lambda_1^2k^4 - k^6) \\ - \beta^2k^2 - \lambda_1^2\lambda_3\lambda_5k^4 + (2\lambda_2k^4 + 2\lambda_1^2\lambda_2k^2)\tau^{-1} \end{bmatrix} \\
- U_m(U_m - U_T)(2\lambda_1^2\lambda_2k^3 + 2\lambda_2k^5) + U_T(U_m - U_T)(2\lambda_1^2\lambda_2k^3 - 2\lambda_2k^5) \\
+2(U_m - U_T)\beta\lambda_2k^3 + U_m\lambda_1^2\lambda_3\lambda_4k^3 + U_T\lambda_1^2\lambda_3\lambda_4k^3 - \beta\lambda_1^2\lambda_3\lambda_4k - U_m^2(k^5 + 2\lambda_1^2k^3)\tau^{-1} \\
+U_T^2(k^5 - 2\lambda_1^2k^3)\tau^{-1} + U_m\beta(2k^3 + 2\lambda_1^2k)\tau^{-1} - \beta^2k\tau^{-1}
\end{array}
\right\}
$$

$$= 0.$$

Let the real and imaginary parts of the left-hand side of the dispersion equation be zero, yielding two separate equations:

$$
\begin{aligned}
&(c_r^3 - 3c_rc_i^2)(2\lambda_1^2k^4 + k^6) - c_r^2[(U_m - U_T)(2\lambda_1^2k^4 + k^6) + U_m(4\lambda_1^2k^4 + 2k^6) - (2\beta\lambda_1^2k^2 + 2\beta k^4)] \\
&+ c_i^2[(U_m - U_T)(2\lambda_1^2k^4 + k^6) + U_m(4\lambda_1^2k^4 + 2k^6) - (2\beta\lambda_1^2k^2 + 2\beta k^4)] - 2c_rc_i[(2\lambda_1^2\lambda_2k^3 + 2\lambda_2k^5) + (k^5 + 2\lambda_1^2k^3)\tau^{-1}] \\
&+ c_r\begin{bmatrix} U_m(U_m - U_T)(4\lambda_1^2k^4 + 2k^6) - (U_m - U_T)\beta(2\lambda_1^2k^2 + 2k^4) \\ + U_m^2(2\lambda_1^2k^4 + k^6) + U_T^2(2\lambda_1^2k^4 - k^6) - U_m\beta(2\lambda_1^2k^2 + 2k^4) \\ + \beta^2k^2 + \lambda_1^2\lambda_3\lambda_5k^4 - (2\lambda_2k^4 + 2\lambda_1^2\lambda_2k^2)\tau^{-1} \end{bmatrix} \\
&+ c_i\begin{bmatrix} (U_m - U_T)(2\lambda_1^2\lambda_2k^3 + 2\lambda_2k^5) + U_m(2\lambda_1^2\lambda_2k^3 + 2\lambda_2k^5) - U_T(2\lambda_1^2\lambda_2k^3 - 2\lambda_2k^5) \\ - 2\beta\lambda_2k^3 - \lambda_1^2\lambda_3\lambda_4k^3 + U_m(2k^5 + 4\lambda_1^2k^3)\tau^{-1} - \beta(2k^3 + 2\lambda_1^2k)\tau^{-1} \end{bmatrix} \\
&- U_m^2(U_m - U_T)(2\lambda_1^2k^4 + k^6) - U_T^2(U_m - U_T)(2\lambda_1^2k^4 - k^6) + U_m(U_m - U_T)\beta(2\lambda_1^2k^2 + 2k^4) - (U_m - U_T)\beta^2k^2 \\
&- U_m\lambda_1^2\lambda_3\lambda_5k^4 - U_T\lambda_1^2\lambda_3\lambda_5k^4 + \beta\lambda_1^2\lambda_3\lambda_5k^2 + U_m(2\lambda_2k^4 + 2\lambda_1^2\lambda_2k^2)\tau^{-1} + U_T(2\lambda_2k^4 - 2\lambda_1^2\lambda_2k^2)\tau^{-1} - 2\beta\lambda_2k^2\tau^{-1} \\
&= 0,
\end{aligned}
$$

and

$$
\begin{aligned}
&(c_i^3 - 3c_r^2c_i)(2\lambda_1^2k^4 + k^6) - c_r^2[(2\lambda_1^2\lambda_2k^3 + 2\lambda_2k^5) + (k^5 + 2\lambda_1^2k^3)\tau^{-1}] + c_i^2[(2\lambda_1^2\lambda_2k^3 + 2\lambda_2k^5) + (k^5 + 2\lambda_1^2k^3)\tau^{-1}] \\
&+ 2c_rc_i[(U_m - U_T)(2\lambda_1^2k^4 + k^6) + U_m(4\lambda_1^2k^4 + 2k^6) - (2\beta\lambda_1^2k^2 + 2\beta k^4)] \\
&+ c_r\begin{bmatrix} (U_m - U_T)(2\lambda_1^2\lambda_2k^3 + 2\lambda_2k^5) + U_m(2\lambda_1^2\lambda_2k^3 + 2\lambda_2k^5) - U_T(2\lambda_1^2\lambda_2k^3 - 2\lambda_2k^5) \\ - 2\beta\lambda_2k^3 - \lambda_1^2\lambda_3\lambda_4k^3 + U_m(2k^5 + 4\lambda_1^2k^3)\tau^{-1} - \beta(2k^3 + 2\lambda_1^2k)\tau^{-1} \end{bmatrix} \\
&- c_i\begin{bmatrix} U_m(U_m - U_T)(4\lambda_1^2k^4 + 2k^6) - (U_m - U_T)\beta(2\lambda_1^2k^2 + 2k^4) \\ + U_m^2(2\lambda_1^2k^4 + k^6) + U_T^2(2\lambda_1^2k^4 - k^6) - U_m\beta(2\lambda_1^2k^2 + 2k^4) \\ + \beta^2k^2 + \lambda_1^2\lambda_3\lambda_5k^4 - (2\lambda_2k^4 + 2\lambda_1^2\lambda_2k^2)\tau^{-1} \end{bmatrix} \\
&- U_m(U_m - U_T)(2\lambda_1^2\lambda_2k^3 + 2\lambda_2k^5) + U_T(U_m - U_T)(2\lambda_1^2\lambda_2k^3 - 2\lambda_2k^5) \\
&+ 2(U_m - U_T)\beta\lambda_2k^3 + U_m\lambda_1^2\lambda_3\lambda_4k^3 + U_T\lambda_1^2\lambda_3\lambda_4k^3 - \beta\lambda_1^2\lambda_3\lambda_4k \\
&- U_m^2(k^5 + 2\lambda_1^2k^3)\tau^{-1} + U_T^2(k^5 - 2\lambda_1^2k^3)\tau^{-1} + U_m\beta(2k^3 + 2\lambda_1^2k)\tau^{-1} - \beta^2k\tau^{-1} \\
&= 0.
\end{aligned}
$$

Defining

$$\varepsilon_1 = 2\lambda_1^2 k^4 + k^6,$$

$$\varepsilon_2 = (U_m - U_T)(2\lambda_1^2 k^4 + k^6) + U_m(4\lambda_1^2 k^4 + 2k^6) - (2\beta\lambda_1^2 k^2 + 2\beta k^4),$$

$$\varepsilon_3 = 2\lambda_1^2\lambda_2 k^3 + 2\lambda_2 k^5 + (k^5 + 2\lambda_1^2 k^3)\tau^{-1},$$

$$\varepsilon_4 = U_m(U_m - U_T)(4\lambda_1^2 k^4 + 2k^6) - (U_m - U_T)\beta(2\lambda_1^2 k^2 + 2k^4) + U_m^2(2\lambda_1^2 k^4 + k^6) + U_T^2(2\lambda_1^2 k^4 - k^6) - U_m\beta(2\lambda_1^2 k^2 + 2k^4) + \beta^2 k^2 + \lambda_1^2\lambda_3\lambda_5 k^4 - (2\lambda_2 k^4 + 2\lambda_1^2\lambda_2 k^2)\tau^{-1},$$

$$\varepsilon_5 = (U_m - U_T)(2\lambda_1^2\lambda_2 k^3 + 2\lambda_2 k^5) + U_m(2\lambda_1^2\lambda_2 k^3 + 2\lambda_2 k^5) - U_T(2\lambda_1^2\lambda_2 k^3 - 2\lambda_2 k^5) - 2\beta\lambda_2 k^3 - \lambda_1^2\lambda_3\lambda_4 k^3 + U_m(2k^5 + 4\lambda_1^2 k^3)\tau^{-1} - \beta(2k^3 + 2\lambda_1^2 k)\tau^{-1},$$

$$\varepsilon_6 = -U_m^2(U_m - U_T)(2\lambda_1^2 k^4 + k^6) - U_T^2(U_m - U_T) \times (2\lambda_1^2 k^4 - k^6) + U_m(U_m - U_T) \times \beta(2\lambda_1^2 k^2 + 2k^4) - (U_m - U_T)\beta^2 k^2 - U_m\lambda_1^2\lambda_3\lambda_5 k^4 - U_T\lambda_1^2\lambda_3\lambda_5 k^4 + \beta\lambda_1^2\lambda_3\lambda_5 k^2 + U_m(2\lambda_2 k^4 + 2\lambda_1^2\lambda_2 k^2)\tau^{-1} + U_T(2\lambda_2 k^4 - 2\lambda_1^2\lambda_2 k^2)\tau^{-1} - 2\beta\lambda_2 k^2\tau^{-1},$$

$$\varepsilon_7 = -U_m(U_m - U_T)(2\lambda_1^2\lambda_2 k^3 + 2\lambda_2 k^5) + U_T(U_m - U_T) \times (2\lambda_1^2\lambda_2 k^3 - 2\lambda_2 k^5) + 2(U_m - U_T)\beta\lambda_2 k^3 + U_m\lambda_1^2\lambda_3\lambda_4 k^3 + U_T\lambda_1^2\lambda_3\lambda_4 k^3 - \beta\lambda_1^2\lambda_3\lambda_4 k - U_m^2(k^5 + 2\lambda_1^2 k^3)\tau^{-1} + U_T^2(k^5 - 2\lambda_1^2 k^3)\tau^{-1} + U_m\beta(2k^3 + 2\lambda_1^2 k)\tau^{-1} - \beta^2 k\tau^{-1},$$

one may obtain the final dispersion equations for c_r and c_i:

$$\varepsilon_1 c_r^3 - 3\varepsilon_1 c_r c_i^2 - \varepsilon_2 c_r^2 + \varepsilon_2 c_i^2 - 2\varepsilon_3 c_r c_i + \varepsilon_4 c_r + \varepsilon_5 c_i + \varepsilon_6 = 0,$$

$$\varepsilon_1 c_i^3 - 3\varepsilon_1 c_r^2 c_i - \varepsilon_3 c_r^2 + \varepsilon_3 c_i^2 + 2\varepsilon_2 c_r c_i + \varepsilon_5 c_r - \varepsilon_4 c_i + \varepsilon_7 = 0.$$

REFERENCES

Adames, Á. F., and Y. Ming, 2018: Interactions between water vapor and potential vorticity in synoptic-scale monsoonal disturbances: Moisture vortex instability. *J. Atmos. Sci.*, **75**, 2083–2106, https://doi.org/10.1175/JAS-D-17-0310.1.

Betts, A. K., 1986: A new convective adjustment scheme. Part I: Observational and theoretical basis. *Quart. J. Roy. Meteor. Soc.*, **112**, 667–691, https://doi.org/10.1002/qj.49711247307.

——, and M. J. Miller, 1986: A new convective adjustment scheme. Part II: Single column tests using GATE wave, BOMEX, ATEX and arctic air-mass data sets. *Quart. J. Roy. Meteor. Soc.*, **112**, 693–709, https://doi.org/10.1002/qj.49711247308.

Bretherton, C., M. Peters, and L. Back, 2004: Relationships between water vapor path and precipitation over the tropical oceans. *J. Climate*, **17**, 1517–1528, https://doi.org/10.1175/1520-0442(2004)017<1517:RBWVPA>2.0.CO;2.

Charney, J. G., 1947: The dynamics of long waves in a baroclinic westerly current. *J. Meteor.*, **4**, 135–162, https://doi.org/10.1175/1520-0469(1947)004<0136:TDOLWI>2.0.CO;2.

Chen, G. T. J., and C.-P. Chang, 1980: The structure and vorticity budget of an early summer monsoon trough (mei-yu) over southeastern China and Japan. *Mon. Wea. Rev.*, **108**, 942–953, https://doi.org/10.1175/1520-0493(1980)108<0942:TSAVBO>2.0.CO;2.

Choi, J. W., H. D. Kim, and B. Wang, 2020: Interdecadal variation of changma (Korean summer monsoon rainy season) retreat date in Korea. *Int. J. Climatol.*, **40**, 1348–1360, https://doi.org/10.1002/joc.6272.

Cohen, N. Y., and W. R. Boos, 2016: Perspectives on moist baroclinic instability: Implications for the growth of monsoon depressions. *J. Atmos. Sci.*, **73**, 1767–1788, https://doi.org/10.1175/JAS-D-15-0254.1.

Day, J. A., I. Fung, and W. Liu, 2018: Changing character of rainfall in eastern China, 1951–2007. *Proc. Natl. Acad. Sci. USA*, **115**, 2016–2021, https://doi.org/10.1073/pnas.1715386115.

Ding, Y. H., 1992: Summer monsoon rainfall in China. *J. Meteor. Soc. Japan*, **70**, 373–396, https://doi.org/10.2151/jmsj1965.70.1B_373.

——, 2007: The variability of the Asian summer monsoon. *J. Meteor. Soc. Japan*, **85B**, 21–54, https://doi.org/10.2151/jmsj.85B.21.

Eady, E. T., 1949: Long waves and cyclone waves. *Tellus*, **1**, 33–52, https://doi.org/10.3402/tellusa.v1i3.8507.

Emanuel, K. A., M. Fantini, and A. J. Thorpe, 1987: Baroclinic instability in an environment of small stability to slantwise moist convection. *J. Atmos. Sci.*, **44**, 1559–1573, https://doi.org/10.1175/1520-0469(1987)044<1559:BIIAEO>2.0.CO;2.

Fantini, M., 1993: A numerical study of two-dimensional moist baroclinic instability. *J. Atmos. Sci.*, **50**, 1199–1210, https://doi.org/10.1175/1520-0469(1993)050<1199:ANSOTD>2.0.CO;2.

Fowlis, W. W., and R. Hide, 1965: Thermal convection in a rotating annulus of liquid: Effect of viscosity on the transition between axisymmetric and non-axisymmetric flow regimes. *J. Atmos. Sci.*, **22**, 541–558, https://doi.org/10.1175/1520-0469(1965)022<0541:TCIARA>2.0.CO;2.

Gao, S. T., Y. S. Zhou, and T. Lei, 2002: Structural features of the meiyu front system. *J. Meteor. Res.*, **16**, 195–204.

Hersbach, H., and Coauthors, 2019: Global reanalysis: Goodbye ERA-Interim, hello ERA5. *ECMWF Newsletter*, No. 159, ECMWF, Reading, United Kingdom, 17–24, https://www.ecmwf.int/node/19027.

Holton, J. R., 2004: *An Introduction to Dynamic Meteorology*. 4th ed. Elsevier Academic Press, 535 pp.

Hu, Y., Y. Deng, Y. Lin, Z. Ming, C. Cui, and X. Dong, 2021: Dynamics of the spatiotemporal morphology of Mei-Yu fronts: An initial survey. *Climate Dyn.*, **56**, 2715–2728, https://doi.org/10.1007/s00382-020-05619-2.

Huffman, G. J., R. F. Adler, M. M. Morrissey, D. T. Bolvin, S. Curtis, R. Joyce, B. McGavock, and J. Susskind, 2001: Global

precipitation at one-degree daily resolution from multisatellite observations. *J. Hydrometeor.*, **2**, 36–50, https://doi.org/10.1175/1525-7541(2001)002<0036:GPAODD>2.0.CO;2.

Jiang, X., and Coauthors, 2015: Vertical structure and physical processes of the Madden-Julian Oscillation: Exploring key model physics in climate simulations. *J. Geophys. Res. Atmos.*, **120**, 4718–4748, https://doi.org/10.1002/2014JD022375.

Li, T., 2006: Origin of the summertime synoptic-scale wave train in the western North Pacific. *J. Atmos. Sci.*, **63**, 1093–1102, https://doi.org/10.1175/JAS3676.1.

Liu, F., and B. Wang, 2017: Effects of moisture feedback in a frictional coupled Kelvin-Rossby wave model and implication in the Madden–Julian Oscillation dynamics. *Climate Dyn.*, **48**, 513–522, https://doi.org/10.1007/s00382-016-3090-y.

Liu, J. J., Y. H. Ding, and J. H. He, 2003: The structure analysis of a typical meiyu front (in Chinese). *Acta Meteor. Sin.*, **61**, 291–303.

Mak, M., 1982: On moist quasi-geostrophic baroclinic instability. *J. Atmos. Sci.*, **39**, 2028–2037, https://doi.org/10.1175/1520-0469(1982)039<2028:OMQGBI>2.0.CO;2.

Nie, J., A. H. Sobel, D. A. Shaevitz, and S. Wang, 2018: Dynamic amplification of extreme precipitation sensitivity. *Proc. Natl. Acad. Sci. USA*, **115**, 9467–9472, https://doi.org/10.1073/pnas.1800357115.

Pedlosky, J., 1964: An initial value problem in the theory of baroclinic instability. *Tellus*, **16**, 12–17, https://doi.org/10.3402/tellusa.v16i1.8892.

Phillips, N. A., 1954: Energy transformations and meridional circulations associated with simple baroclinic waves in a two-level, quasi-geostrophic model. *Tellus*, **6**, 273–286, https://doi.org/10.1111/j.2153-3490.1954.tb01123.x.

Smagorinsky, J. S., S. Manabe, and J. L. Holloway, 1965: Numerical results from a nine-level general circulation model of the atmosphere. *Mon. Wea. Rev.*, **93**, 727–768, https://doi.org/10.1175/1520-0493(1965)093<0727:NRFANL>2.3.CO;2.

Sobel, A. H., J. Nilsson, and L. M. Polvani, 2001: The weak temperature gradient approximation and balanced tropical moisture waves. *J. Atmos. Sci.*, **58**, 3650–3665, https://doi.org/10.1175/1520-0469(2001)058<3650:TWTGAA>2.0.CO;2.

Wang, B., and A. Barcilon, 1986: Moist stability of a baroclinic zonal flow with conditionally unstable stratification. *J. Atmos. Sci.*, **43**, 705–719, https://doi.org/10.1175/1520-0469(1986)043<0705:MSOABZ>2.0.CO;2.

——, and T. Li, 1993: A simple tropical atmosphere model of relevance to short-term climate variations. *J. Atmos. Sci.*, **50**, 260–284, https://doi.org/10.1175/1520-0469(1993)050<0260:ASTAMO>2.0.CO;2.

——, and H. Lin, 2002: Rainy season of the Asian–Pacific summer monsoon. *J. Climate*, **15**, 386–398, https://doi.org/10.1175/1520-0442(2002)015<0386:RSOTAP>2.0.CO;2.

——, and G. Chen, 2017: A general theoretical framework for understanding essential dynamics of Madden–Julian Oscillation. *Climate Dyn.*, **49**, 2309–2328, https://doi.org/10.1007/s00382-016-3448-1.

——, A. Barcilon, and L. N. Howard, 1985: Linear dynamics of transient planetary waves in the presence of damping. *J. Atmos. Sci.*, **42**, 1893–1910, https://doi.org/10.1175/1520-0469(1985)042<1893:LDOTPW>2.0.CO;2.

——, S. Clemens, and P. Liu, 2003: Contrasting the Indian and East Asian monsoons: Implications on geologic time scale. *Mar. Geol.*, **201**, 5–21, https://doi.org/10.1016/S0025-3227(03)00196-8.

Wang, L., T. Li, E. Maloney, and B. Wang, 2017: Fundamental causes of propagating and nonpropagating MJOs in MJOTF/GASS models. *J. Climate*, **30**, 3743–3769, https://doi.org/10.1175/JCLI-D-16-0765.1.

Yue, C. J., S. W. Shou, K. P. Lin, and X. P. Yao, 2003: Diagnosis of the heavy rain near a meiyu front using the wet Q vector partitioning method. *Adv. Atmos. Sci.*, **20**, 37–44, https://doi.org/10.1007/BF03342048.

Zhao, C., and T. Li, 2019: Basin dependence of the MJO modulating tropical cyclone genesis. *Climate Dyn.*, **52**, 6081–6096, https://doi.org/10.1007/s00382-018-4502-y.